



HAL
open science

Energy Flux and Characteristic Energy of Electrons Over Jupiter's Main Auroral Emission

F. Allegrini, B. Mauk, G. Clark, G. R. Gladstone, V. Hue, W. S. Kurth, F. Bagenal, S. Bolton, B. Bonfond, J. E. P. Connerney, et al.

► **To cite this version:**

F. Allegrini, B. Mauk, G. Clark, G. R. Gladstone, V. Hue, et al.. Energy Flux and Characteristic Energy of Electrons Over Jupiter's Main Auroral Emission. *Journal of Geophysical Research Space Physics*, 2020, 125, 10.1029/2019JA027693 . insu-03673156

HAL Id: insu-03673156

<https://insu.hal.science/insu-03673156>

Submitted on 20 May 2022

HAL is a multi-disciplinary open access archive for the deposit and dissemination of scientific research documents, whether they are published or not. The documents may come from teaching and research institutions in France or abroad, or from public or private research centers.

L'archive ouverte pluridisciplinaire **HAL**, est destinée au dépôt et à la diffusion de documents scientifiques de niveau recherche, publiés ou non, émanant des établissements d'enseignement et de recherche français ou étrangers, des laboratoires publics ou privés.

Copyright

JGR Space Physics

RESEARCH ARTICLE

10.1029/2019JA027693

Special Section:

Jupiter Midway Through the Juno Mission

Key Points:

- We present a survey of Jovian auroral electrons characteristics from 50 eV to 1000 keV by Juno
- We present a metric to identify main oval crossings in electron data using 3-30 keV electrons energy flux
- We estimate the UV brightness per incident electron energy flux as a function of characteristic energy

Supporting Information:

- Supporting Information S1

Correspondence to:

F. Allegrini,
fallegrini@swri.edu

Citation:

Allegrini, F., Mauk, B., Clark, G., Gladstone, G. R., Hue, V., Kurth, W. S., et al. (2020). Energy flux and characteristic energy of electrons over Jupiter's main auroral emission. *Journal of Geophysical Research: Space Physics*, 125, e2019JA027693. <https://doi.org/10.1029/2019JA027693>

Received 5 DEC 2019

Accepted 5 MAR 2020

Accepted article online 12 MAR 2020

Energy Flux and Characteristic Energy of Electrons Over Jupiter's Main Auroral Emission

F. Allegrini^{1,2} , B. Mauk³ , G. Clark³ , G. R. Gladstone^{1,2} , V. Hue¹ , W. S. Kurth⁴ , F. Bagenal⁵ , S. Bolton¹ , B. Bonfond⁶ , J. E. P. Connerney^{7,8} , R. W. Ebert^{1,2} , T. Greathouse¹ , M. Imai⁴ , S. Levin⁹ , P. Louarn¹⁰ , D. J. McComas¹¹ , J. Saur¹² , J. R. Szalay¹¹ , P. W. Valek¹ , and R. J. Wilson⁵ 

¹Southwest Research Institute, San Antonio, TX, USA, ²Department of Physics and Astronomy, University of Texas at San Antonio, San Antonio, TX, USA, ³The Johns Hopkins University Applied Physics Laboratory, Laurel, MD, USA,

⁴Department of Physics and Astronomy, University of Iowa, Iowa City, IA, USA, ⁵Laboratory for Atmospheric and Space Physics, University of Colorado Boulder, Boulder, CO, USA, ⁶Laboratoire de Physique Atmosphérique et Planétaire, Université de Liège, Liège, Belgium, ⁷Space Research Corporation, Annapolis, MD, USA, ⁸NASA Goddard Space Flight Center, Greenbelt, MD, USA, ⁹Jet Propulsion Laboratory, Pasadena, CA, USA, ¹⁰Institut de Recherche en Astrophysique et Planétologie (IRAP), Toulouse, France, ¹¹Department of Astrophysical Sciences, Princeton University, Princeton, NJ, USA, ¹²Institute of Geophysics and Meteorology, University of Cologne, Cologne, Germany

Abstract Jupiter's ultraviolet (UV) aurorae, the most powerful and intense in the solar system, are caused by energetic electrons precipitating from the magnetosphere into the atmosphere where they excite the molecular hydrogen. Previous studies focused on case analyses and/or greater than 30-keV energy electrons. Here for the first time we provide a comprehensive evaluation of Jovian auroral electron characteristics over the entire relevant range of energies (~100 eV to ~1 MeV). The focus is on the first eight periapses providing a coarse but complete System III view of the northern and southern auroral regions with corresponding UV observations. The latest magnetic field model JRM09 with a current sheet model is used to map Juno's magnetic foot point onto the UV images and relate the electron measurements to the UV features. We find a recurring pattern where the 3- to 30-keV electron energy flux peaks in a region just equatorward of the main emission. The region corresponds to a minimum of the electron characteristic energy (<10 keV). Its polarward edge corresponds to the equatorward edge of the main oval, which is mapped at M shells of ~51. A refined current sheet model will likely bring this boundary closer to the expected 20–30 R_J . Outside that region, the >100-keV electrons contribute to most (>~70–80%) of the total downward energy flux and the characteristic energy is usually around 100 keV or higher. We examine the UV brightness per incident energy flux as a function of characteristic energy and compare it to expectations from a model.

Plain Language Summary Aurorae, also commonly called Northern or Southern Lights, are among the most spectacular displays of nature. They are observed not only at Earth but at other planets too, such as Mars, Jupiter, and Saturn. In fact, Jupiter has the brightest aurora in the solar system. The aurora is created when electrons and/or ions in space precipitate into the atmosphere and excite the ambient gas. At Jupiter, they mostly shine in the ultraviolet which is invisible to our eyes but can be seen with suitable instrumentation. The faster the electrons, the deeper they go into the atmosphere, but also the more energy they carry, which eventually can be converted to create more light. This study is about characterizing the electrons that create Jupiter's aurora using many instruments from the National Aeronautics and Space Administration's Juno Mission. We find that different ultraviolet emissions correspond to different electron characteristics. Knowing the differences will help us to understand the bigger picture to explain the processes that create the aurora.

1. Introduction

Prior to Juno, studies of the Jovian aurora were primarily based on remote observations from Earth-orbiting observatories, such as Hubble Space Telescope (HST), Chandra, and XMM-Newton X-ray Observatories (Clarke et al., 2004; Dunn et al., 2017; Gérard et al., 2016; Gladstone et al., 2002; Grodent et al., 2003; Gustin et al., 2016; Nichols et al., 2009; Waite et al., 2000) and ground-based observatories, such as the Infrared Telescope Facility (Clarke et al., 2004). These data provided the basis for our phenomenological

understanding of the complex and dynamic nature of the brightest UV aurora in the solar system. Grodent (2015) reviewed the numerous types of auroral behavior and outlined the importance of in situ observations to uncover the causal links between magnetospheric phenomenon and their auroral manifestations. Jupiter's main auroral emission is much more intense and less variable than the Earth's aurora. The relatively steady, narrow (couple degrees or few thousand kilometers wide) main aurora is an indication of the plasma in the magnetosphere being coupled to Jupiter's 10-hr spin (Cowley & Bunce, 2001; Hill, 2001).

The main emissions create a clear landmark to define the different regions of the Jovian aurora. The emissions located outside this statistical oval map to distance from 6 to $\sim 30 R_J$ in the magnetosphere. They are made of diffuse emissions (Radioti et al., 2009), more compact patches of emissions (Dumont et al., 2014), secondary arcs (Gray et al., 2017), and satellite footprints (Bonfond et al., 2012). The main emissions themselves, generally mapping from 20 to $60 R_J$, are rarely made of a continuous oval but rather of a discontinuous set of arcs (Radioti et al., 2008), often brighter at dusk than at dawn (Bonfond et al., 2015). However, at times, the dawn arc can become extremely bright and form a so-called dawn storm (Gustin et al., 2006; Kimura et al., 2017). The polar-most region can be divided into three subregions (Grodent, Clarke, Waite, et al., 2003): the swirl region in the center, possibly corresponding to field lines open to the solar wind, the active region in the noon and dusk part, and the dark region on the dawn flank. In average, the outer, main and polar emissions each account for approximately one third of the total emitted power (Grodent et al., 2018). However, the auroral types respond very differently to the solar wind input, with the polar and main emission brightening during compressed intervals while the outer emissions appear unaffected (Nichols et al., 2017, 2007, 2009). On the other hand, the outer emissions appear to brighten in response to internally driven reconfigurations (Bonfond et al., 2012; Kimura et al., 2015). In a recent study, Yao et al. (2019) used HST and Hisaki observations, as well as in situ measurements of particles, magnetic field, and radio waves from Juno, to show that the dynamics of the middle magnetosphere are coupled with auroral variability.

The electrons that excite aurora in the atmosphere carry electrical currents. Hill (1979) first proposed that Jupiter's aurora currents connect fresh plasma in the magnetosphere to the planet's rotation ionosphere (see review by Bagenal et al., 2017). As the equatorial plasma is transported radially outward these coupling currents, keep the plasma accelerated up to corotation. At some point the coupling breaks down and the plasma deviates from rigid corotation. As Hill (1979) noted, this corotation breakdown distance is where the currents are strongest and the corresponding aurora brightest. McNutt et al. (1979) reported that Voyager plasma measurements found this deviation from corotation at $\sim 17\text{--}20 R_J$. Subsequent models examined what factors could be limiting the angular momentum transfer to the plasma disk: some (e.g., Nichols & Cowley, 2004) suggested the electrical conductivity of the ionosphere; others (e.g., Huang & Hill, 1989) invoked weak coupling of the ionosphere to the deep atmosphere, while terrestrial auroral experience evoked the concept of voltage structures developing above the ionosphere where the low density of electrons limits the currents flowing along the magnetic field (e.g., Ray et al., 2010). Mauk and Saur (2007) showed that in situ particle measurements by the Galileo spacecraft revealed the auroral currents to be highly structured and variable as they flowed up and down along field lines. Saur et al. (2003) proposed turbulence to be the primary mechanism for converting kinetic energy in the plasma disk to power the main aurora. To determine which processes are driving Jupiter's aurora fields and particle measurements is needed over Jupiter's polar region.

Before there were in situ particle measurements in the auroral region, remote observations had to rely on the atmospheric modeling and spectral analysis of the UV to determine the characteristics of the precipitating electrons (e.g., Gustin et al., 2004). Color ratios—the ratio of the unabsorbed UV intensity and the absorbed UV intensity—provide a proxy for the penetration depth of the electrons. The basic idea is that more energetic electrons will penetrate deeper into the atmosphere and be characterized by a higher color ratio from higher methane absorption deep in the atmosphere. This ratio is also a measure of the attenuation of the H_2 emission by hydrocarbons (typically assumed to be methane); therefore, the assumed distribution of hydrocarbons can influence the interpretations of the color ratio. Previous studies have shown that the hydrocarbons in Jupiter's auroral region are enhanced due to much more effective eddy mixing because of the intense auroral energy input from precipitating electrons in the upper atmosphere (Clark et al., 2018; Parkinson et al., 2006). The only region that shows a clear relationship between the UV brightness and the intensity

of the methane absorption (a proxy for the precipitating electron energy) is the main emission (Gérard et al., 2016). The more energetic the precipitating particle, the deeper it deposits its energy. Thus, the column of methane encountered by the emitted photons increases with electron energy. Using models of the auroral atmosphere (e.g., Grodent et al., 2001), it is then possible to relate the color ratio between absorbed and unabsorbed wavelength ranges and the impinging electron energy (e.g., Gustin et al., 2002). It should however be noted that such a relationship depends on a number of hypotheses that are not well constrained (Gustin et al., 2016), which lead some authors to use several models in order to test the sensitivity of the method (Gérard et al., 2014). Therefore, it is critically important to carefully measure the in situ particle environment and compare them to the UV observations to better constrain the atmospheric models used and to further understand the energy flux to brightness relationships.

Juno is the first spacecraft to repeatedly fly over the auroral regions of Jupiter in order to study the particles that create the most intense aurora in the solar system (Bagenal et al., 2017; Bolton et al., 2017; Connerney et al., 2017). The Jovian Auroral Distributions Experiment (JADE, McComas et al., 2017) and the Juno Energetic particle Detector Instrument (JEDI, Mauk et al., 2017) characterize the particle distributions, while at the same time the Ultraviolet Spectrograph (UVS, Gladstone et al., 2017) and the Jovian InfraRed Auroral Mapper (Adriani et al., 2017) image the aurora at ultraviolet and infrared wavelengths. The associated magnetic field is measured by the Juno magnetic field investigation (MAG, Connerney et al., 2017), and the radio and plasma waves are measured by the Waves investigation (Kurth et al., 2017).

Juno's arrival and exploration of Jupiter's polar magnetosphere have revealed new and interesting processes present at the low-altitude, main auroral latitudes. For example, Allegrini et al. (2017) and Mauk, Haggerty, Paranicas, Clark, Kollmann, Rymer, Mitchell et al. (2017) showed that the 100-eV to 1,000-keV electrons in the main auroral region during PJ1 showed a lack of evidence of "inverted V"-type distributions. Subsequent Juno orbits revealed the presence of the inverted V (Clark et al., 2017; Ebert et al., 2017; Louarn et al., 2018; Mauk, Haggerty, Paranicas, Clark, Kollmann, Rymer, Bolton et al., 2017; Mauk et al., 2018). However, these structures do not appear to be the dominant particle signature associated with the brightest aurora (Mauk, Haggerty, Paranicas, Clark, Kollmann, Rymer, Bolton et al., 2017). In contrast, these distributions have been shown to drive the brightest aurora at Earth (Carlson et al., 1998 and references therein). It appears that the broad energy distributions (distributions that lack sharp peaks in energy) are the more common and dominant particle energy signature in the main auroral region (Allegrini et al., 2017; Clark et al., 2018; Mauk, Haggerty, Paranicas, Clark, Kollmann, Rymer, Mitchell et al. (2017); Szalay et al., 2017, 2018). Several authors have suggested that these distributions are indicative of wave-particle accelerations via, say, Alfvén or whistler mode waves (e.g., Elliott et al., 2018; Kurth et al., 2018; Saur et al., 2018).

In this paper, we combine the JADE and JEDI electron data sets from the first eight Juno perijoves, for a total of 16 passes over the main auroral emissions (eight per hemisphere). This study is limited to the first eight perijoves because the spacecraft orientation was most favorable to the particle instrument fields of view (FOVs). While the pitch angle coverage is less optimal for later perijove passes, the features described in this study are also observed later in the mission. The observed energy flux and characteristic energy of precipitating electrons are put into context using UV images and mapping Juno's footprint with the most recent magnetic field model (Connerney et al., 2018). We also examine differences of energy flux and characteristic energy for electrons moving toward and away from Jupiter. We illustrate the changes in the electron energy spectra and the pitch angle distributions as Juno flies over the main auroral emission regions. Finally, we look at the relationship between those quantities and the UV brightness measured at the footprint of the magnetic field line passing through Juno mapped onto Jupiter's atmosphere.

Section 2 of this paper briefly describes the instruments (JADE, JEDI, UVS, and MAG) and the data that are used for this study. It also describes the calculation of the energy flux and the characteristic energy and how we determine the UV brightness along Juno's magnetic track. In section 3, we describe our results. Section 4 provides a summary and discussion of the results of this study. The supporting information material describes the detailed processes and steps used to determine a corrected sensitivity factor for the JADE electron sensors (Text S1). The sensitivity adjustment was based on comparisons with Waves (Kurth et al., 2017)-derived electron densities. We show that the JADE and JEDI electron

intensities and fluxes are usually within a factor of 2 in the overlapping energy range. We show how we combine the JADE and JEDI electron data sets (Text S2).

2. Instruments and Data

2.1. Description of Instruments

JADE consists of two electron sensors and an ion sensor (McComas et al., 2017). JADE-E (for JADE-Electrons) consists of two identical top hat electrostatic energy analyzers that measure electrons from ~ 100 eV (~ 50 eV after Perijove 6 or PJ6) up to ~ 100 keV (in 64 energy steps) with an energy resolution of the order of 10% to 14% at up to 1-s time resolution. Each analyzer has a 120° nonoverlapping FOV in azimuth (Juno's spin plane) and has deflectors to track the direction of the magnetic field up to $\pm 35^\circ$ in elevation up to 40 keV; the deflection is $\sim \pm 15^\circ$ at 100 keV. The angular resolution is $\sim 7.5^\circ$ in azimuth and $\sim 2\text{--}5.5^\circ$ in elevation. A third identical sensor covering the remaining 120° in azimuth was turned off before Juno's arrival at Jupiter due to a high voltage issue. During one third of a spin (spin period ~ 30 s) JADE-E measures the full pitch angle distribution (from 0° to 180°), and during the remaining two thirds, JADE-E measures at least 120° of the full pitch angle range. The magnetic vector components are received every 2 s from the onboard magnetometer (Connerney, Benn, et al., 2017) and are propagated using the spacecraft spin rate to calculate the required deflection angle.

JEDI consists of three high-energy electron and ion telescopes with a fan-like FOV of $\sim 160^\circ$ by 12° (Mauk, Haggerty, Jaskulek, et al., 2017). Two of the telescopes (JEDI-90 and 270) have their FOV tilted by 10° with respect to the spacecraft deck, or spin plane, to avoid looking at the solar panels, and the third telescope has its FOV orientated perpendicular to the spin plane such that it samples a major fraction of 4π sr every spin except for $\sim 12^\circ$ toward the spin axis for sun avoidance. JEDI measures electron distributions from ~ 25 keV up to ~ 1 MeV in 20 energy channels with an angular resolution (pixel) of 9° by 17° . Pitch angle distributions are calculated on the ground using the magnetic field vector measured with Juno's magnetometer.

We derive the magnetic field vector used to calculate the pitch angles from the raw broadcast magnetic field vector from the MAG experiment (Connerney, Benn, et al., 2017). The accuracy of this data product (of the order of $1\text{--}2^\circ$) is sufficient for this study since the JADE-E angular resolution is 7.5° .

UVS is an ultraviolet spectrograph imager with a band pass of $68 < \lambda < 210$ nm and a spectral resolution of ~ 2.2 nm (Gladstone et al., 2017; Greathouse et al., 2013). The instrument slit has the shape of a "dog bone," and its long axis is parallel to the spin axis. An image is reconstructed every spin as the FOV is swept across the auroral region. A flat scan mirror situated near the entrance of the telescope is used to observe at up to $\pm 30^\circ$ perpendicular to the Juno spin plane. The spectral information is used to characterize the depth of the emission.

2.2. Data

The JADE-E background is measured by a separate anode that has the same characteristics (physical size and front-end electronics) as the signal anodes but whose access is blocked such that no electron within the energy passband can reach it. A proportionality factor between background anode and signal anode has been derived using flight data. These factors and the method to estimate the backgrounds are given in the supporting information (Text S4). Future releases of the JADE data will include the background-subtracted signal as well as the background that was subtracted. To convert counts per seconds to differential number flux, we used a corrected sensitivity for JADE-E that is different than the original conversion in the instrument paper by McComas et al. (2017). A detailed analysis of the derivation of the corrected JADE-E sensitivity is given in the supporting information (Text S1).

JEDI and JADE take measurements independently and therefore have different time and energy resolutions. For this study, we used JEDI data at 2-s time resolution. In the overlapping energy range (30 to 100 keV), we match JADE-E's time resolution and energy resolution to that of JEDI. A detailed example illustrating the process and its results is also given in the supporting information (Text S2 and Figure S6). The JADE-E data below 30 keV is still displayed and used at the nominal 1-s time resolution.

We calculate the characteristic energy, E_{char} , and the energy flux, E_{Flux} , using equations (1) and (2) in Clark et al. (2018) (see also Mauk, Haggerty, Paranicas, Clark, Kollmann, Rymer, Mitchell et al. (2017)):

$$E_{char} = \frac{\int_{E_{min}}^{E_{max}} I \cdot E \, dE}{\int_{E_{min}}^{E_{max}} I \, dE}, \quad (1)$$

and

$$E_{Flux} = \pi \int_{E_{min}}^{E_{max}} I \cdot E \, dE, \quad (2)$$

where I is the particle intensity ($(\text{cm}^2 \cdot \text{s} \cdot \text{sr} \cdot \text{keV})^{-1}$), E is the electron energy (keV), E_{min} is the lowest energy channel from JADE, and E_{max} is geometric mean of the highest energy channel for JEDI, and the factor π represents the area-projected-weighted loss cone (see Mauk, Haggerty, Paranicas, Clark, Kollmann, Rymer, Mitchell et al. (2017)). We estimate the width of the loss cone by using the simple relationship $Loss \, Cone \, Angle \sim \text{asin}(1/R^3)^{1/2}$ (see also Mauk, Haggerty, Paranicas, Clark, Kollmann, Rymer, Mitchell et al. (2017)), where R is the Jovicentric distance in Jovian radius.

To determine the UV brightness at Juno's magnetic foot point, we produce maps of UV emissions recorded by UVS as close as possible to the estimated time at which Juno is magnetically connected to the region. Depending on the radiation level experienced by Juno at each perijove and on the Juno-UVS planned pointing, the simultaneity between the in situ particle measurements and the UV emission varies on a perijove basis. We then calculate the integrated UV brightness averaged in a 0.1° -wide field of view (i.e., as seen from Juno) around Juno's magnetic foot point. The spot size resulting from the projection of this field of view onto the surface varies depending on the altitude and the viewing angle. The size of the projected spot affects the brightness. If the auroral structure is smaller than the spot, then the averaging will underestimate the brightness of the structure, since the brightness will be averaged over a larger area. While a smaller field of view could mitigate this effect, it could also compete with the instrument resolution. We find that a radius of 0.1° , corresponding to a spot size (diameter) range from ~ 50 to 270 km, is a good compromise for this study.

In a few cases (e.g., PJ1, PJ3S, PJ5N, PJ7N, and PJ9N, where PJ stands for perijove number and N and S for north and south, respectively), there is no UVS image exactly at the time of the main oval crossing. For those cases, we use images taken temporally close (within approximately minutes) to determine the brightness. Jupiter's main oval emissions are known to be relatively stable over the course of tens of minutes to hours (Grodent et al., 2003; Nichols et al., 2009 HST-STIS). Polar emissions can vary on much shorter timescales, down to tens of seconds in the case of flares (Waite et al., 2001). Thus, while it seems that the brightness of the main emissions does not vary significantly over the time periods studied here, it is important to keep in mind that changes could occur.

Finally, to map the footprint of Juno onto the auroral features, we use the recent JRM09 magnetic field model (Connerney et al., 2018) with a current sheet model (Connerney et al., 1981). For the UV polar projections, we chose a mapping altitude of 400 km above the 1-bar level, which is consistent with previous studies (Clarke et al., 1998).

3. Results

3.1. Electron Distributions Over the Main Oval

Figure 1 shows typical electron distributions for a pass over the main auroral oval. The time interval chosen for this example corresponds to the first main oval crossing in the south after Juno's closest approach to Jupiter for Perijove 6 (or PJ6). Other passes up to PJ9 are also provided in the supporting information (Figures S7 to S21 and Text S3). Table 1 gives the selected time intervals for this study (Columns 1 through 5) with the average loss cone angle (Column 6), as well as other information that will be described further.

Figure 2 shows the context for this pass with (a) a reconstructed UV image in false colors and Juno's magnetic footprint track and (b) Juno's trajectory projected into a magnetic reference frame. The tick marks on the track in (a) are spaced by 15 min, and the blue box corresponds to the time interval displayed in Figure 1 (06:48 to 06:58). The thick part of the blue curve corresponds to the times when the UV image

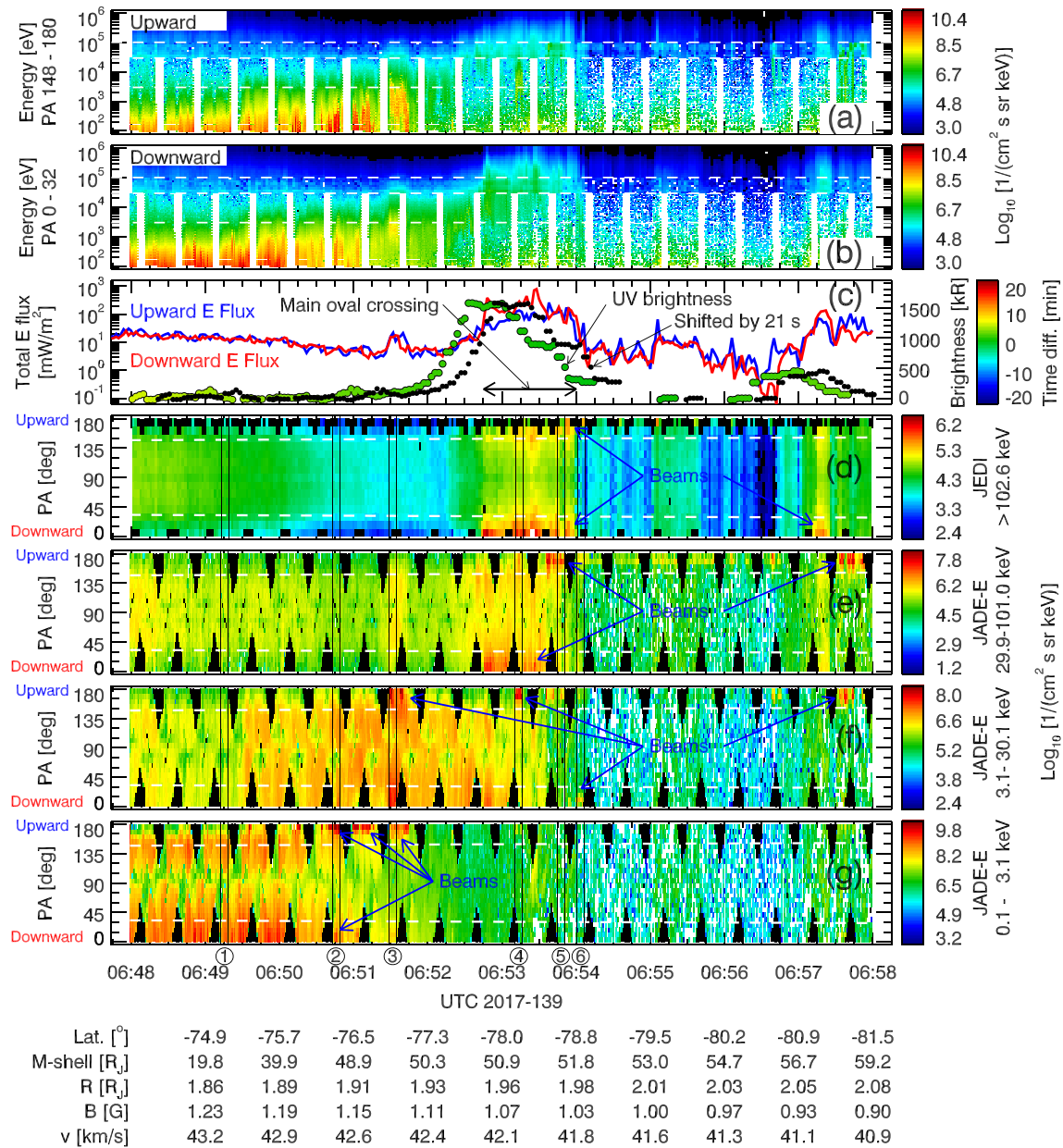


Figure 1. Combined JADE and JEDI electron distributions and UV brightness during the main auroral oval crossing in the south from Perijove 6. Panels (a) and (b) show the electron intensities as a function of time for upward electrons (going away from Jupiter) and downward electrons (going toward Jupiter), respectively. Panel (c) shows the total energy flux within the loss cone of upward and downward electrons, as well as the UV brightness mapped to 400 km altitude using the JRM09 magnetic field model. A 21-s shift of the brightness data lines up very well with the downward energy flux data. We estimate that the main oval crossing happens roughly between 06:52:45 and 06:54:00, which corresponds to the bright white arc in Figure 2a. Juno is in the polar region after 06:54:00. Panels (d) through (g) show the pitch angle distributions for the energy ranges indicated on the right. Some angle beams are shown with blue arrows. The jovigraphic latitude (Lat.), the *M* shell (JRM09+CAN1981), the Jovicentric distance (*R*), the measured magnetic field strength (*B*), and the spacecraft speed (*v*) are indicated at the minute markers at the bottom of the figure. The vertical lines in panels (d) through (g) and the circled numbers below panel (g) indicate time intervals for energy spectra and pitch angle distributions described further.

was collected, and the orange arc shows the direction of the Sun during that same time interval. Panel (b) indicates some *M* shells that are crossed during the pass. We use the terminology “*M* shell” (*M* for magnetic) as an alternative for *L* shell due to the fact that the equatorial crossing distances are strongly affected by the stretched magnetic field lines in the equatorial region of Jupiter’s magnetosphere and deviate from the traditional dipole picture. The *M* shell distance mapping is derived using JRM09 and a current sheet model (Connerney et al., 1981, 1998, 2018), hereafter abbreviated as JRM09+CAN1981.

Table 1
Selected Time Intervals for This Study (Columns 1 Through 5) and Average Loss Cone Angle (Column 6)

PJ	Hemisphere	Date	Time intervals of this study		Average loss cone angle (deg)	Juno local time (hr)	Auroral family type	Time intervals for peak of 3–30 keV E flux		Radial distance (R_J)		M shell (R_J) (JRM09+CAN1981)	
			Start	Stop				Start	Stop	Min	Max	Min	Max
1	North	2016-240	12:08	12:16	37.9	17.8	i	12:10:15	12:13:45	1.60	1.68	13.0	50.1
1	South	2016-240	13:25	13:35	36.8	17.9	i	13:27:45	13:33:15	1.60	1.73	13.3	51.2
3	North	2016-346	16:22	16:29	37.9	17.4	U	16:22:45	16:25:15	1.64	1.69	17.9	50.7
3	South	2016-346	17:34	17:39	40	17.3	U	17:35:45	17:37:45	1.49	1.54	15.7	51.0
4	North	2017-033	12:23	12:29	42.8	17.2	i	12:24:15	12:26:45	1.46	1.51	20.8	51.5
4	South	2017-033	13:32	13:41	36.5	17.0	i	13:36:15	13:39:00	1.65	1.71	17.4	50.4
5	North	2017-086	08:27	08:34	51.6	16.9	I	08:29:45	08:31:45	1.25	1.28	21.0	52.2
5	South	2017-086	09:35	09:49	31.7	16.4	I	09:39:30	09:44:30	1.85	1.97	27.2	52.8
6	North	2017-139	05:27	05:36	44.6	16.9	N	05:29:00	05:32:00	1.42	1.48	39.5	51.3
6	South	2017-139	06:48	06:58	32.2	16.0	N	06:49:15	06:52:45	1.87	1.95	24.2	50.7
7	North	2017-192	01:13	01:21	38.3	17.8	I	01:16:00	01:19:15	1.56	1.64	14.0	50.5
7	South	2017-192	02:27	02:37	38.1	16.0	I	02:29:45	02:33:45	1.55	1.65	15.5	50.9
8	North	2017-244	21:14	21:21	43.3	16.8	U	21:15:15	21:17:45	1.47	1.52	20.5	51.1
8	South	2017-244	22:22	22:30	38.9	15.6	U	22:26:15	22:28:15	1.61	1.65	20.9	50.9
9	North	2017-297	17:16	17:23	51.7	16.2	Q	17:18:45	17:21:15	1.27	1.31	9.7	52.8
9	South	2017-297	18:26	18:40	31.6	14.9	Q	18:30:15	18:34:30	1.85	1.95	23.7	51.6

Note. Juno’s local time in the middle of the interval (Column 7). Auroral family type according to Grodent et al. (2018) in Column 8: Q = “Quiet”; U = “Unsettled”; N = “Narrow”; i = “injections”; I = “strong Injections”; and X = “eXternal perturbation”. The time intervals where the 3- to 30-keV electron energy flux peaks is indicated in Columns 9 and 10 and corresponding radial distances and M shell in Columns 11 through 14. The M shell was calculated using JRM09+CAN1981 (Connerney et al., 1981, 2018, 1998)

Figures 1a and 1b show the combined JADE and JEDI differential number flux (or intensity) as a function of energy and time for upward (going away from Jupiter) and downward (going toward Jupiter) electrons, respectively. The intensity is calculated for the electrons within the loss cone (pitch angle range indicated in the y axis label; see also Column 6 of Table 1). The data from JADE and JEDI have been merged between 30 and 100 keV (see section 2 and supporting information Text S2 and Figure S6 for more information). The white dashed horizontal lines indicate values of 3, 30, and 100 keV.

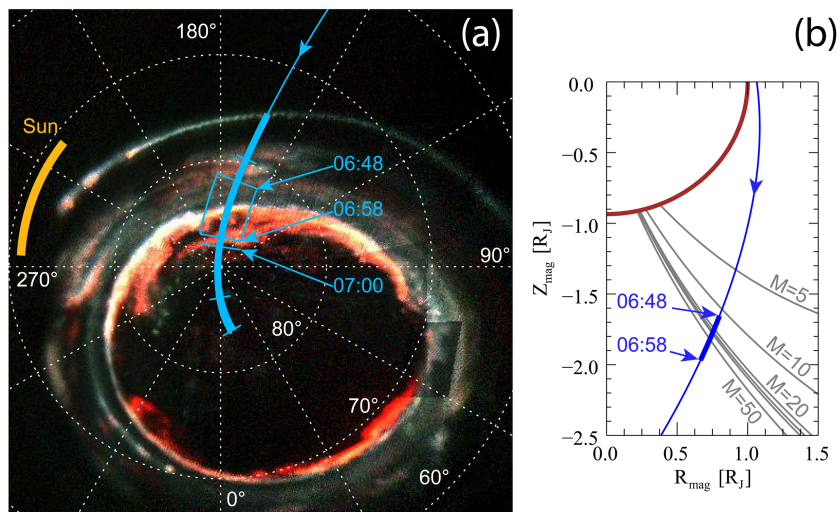


Figure 2. (a) Polar projection of aurora with magnetic footprint track of Juno in light blue. The UV image was taken during the thick part of the track. The time interval of Figure 1 corresponds to the blue box. The tick marks on the blue track are 15 min apart. The thick orange arc shows the direction to the Sun during the integration of the image. (b) Juno’s trajectory in blue shown in a magnetic reference frame. The thick part of the trajectory is for the time interval of Figure 1. The gray lines represent the M shells of 50, 40, 30, 20, 10, and 5 (JRM09+CAN1981). The dark red curve shows the 1-bar level of Jupiter’s atmosphere.

Panel (c) shows the total energy flux of the upward (blue) and downward (red) electrons that are in the loss cone. The colored dots (yellow green for this interval) show the UV brightness along the track (scale on the right), and the color of the dots corresponds to the time difference between when Juno was connected to that particular spot and the average time when the frames for that spot were acquired (color bar on the right). For this particular crossing, the time difference is less than 5 min. The brightness peak corresponds to the main oval crossing (Figure 2a). By shifting the UV brightness data by 21 s, we find a better match with the downward electron energy flux curve. To determine this time shift, we calculate the Spearman's rank correlation between the UV brightness and the total downward energy flux for different time shifts of the UV brightness data. We also limit the correlation calculation to times when the brightness is greater than 20% of the peak brightness. We retain the time shift that gives the highest correlation.

The time shift is not unexpected and can be attributed to the following. The mapping relies on the magnetic field model. While the latest model is much more accurate than previous models, it may still contain some uncertainties in the exact location of Juno's magnetic footprint from higher-order effects not yet accounted for. Thus, spatial foot point mapping errors along the trajectories translate into time shifts.

Panels (d) through (g) show the pitch angle distributions of electrons for the energy ranges indicated to the right of the panels and also separated by the white dashed lines in panels (a) and (b). The black areas correspond to pitch angles that are outside JADE or JEDI's FOV. The white areas in the JADE spectrograms usually correspond to times when the penetrating radiation is high in comparison to the signal, and the background subtraction process removes most of the raw signal (which contains the signal and the background). The vertical lines and the circled numbers below panel (g) define time intervals for energy spectra and pitch angle distributions described further.

In Figure 1, the absolute latitude, the M shell, and the altitude increase from left to right. At the beginning of the interval, the electron intensities are dominated by the <3 keV population (panel (g)). There is a clear empty upward loss cone (pitch angles near 180°) and a full downward loss cone (pitch angles near 0°) indicating that the downward going electrons precipitate into Jupiter's atmosphere and do not mirror back. This is also when we see the loss cone of the low-energy magnetospheric ions reported by Valek et al. (2019).

At around 06:49:15, the intensity of the 3- to 30-keV electrons increases and an empty upward loss cone and a full downward loss cone are also visible. Roughly at the same time, upward electron angle beams sporadically appear in the lowest energies (panel (g)). These upward beams become more frequent until about 06:51:45 when they are no longer seen in the lowest energies. They are, however, seen in the 3- to 30-keV energy range and even later (i.e., at higher latitudes and M shells) in the 30- to 100-keV and >100-keV ranges.

The intensity of >30 keV electrons (panels (d) and (e)) increases at the main oval crossing (~06:52:45 to ~06:54:00). Downward electron angle beams are visible in all four energy ranges throughout the pass, but similar to the upward beams, they are seen in the lower energies at lower latitudes (and M shells) and in the higher energies at higher latitudes (and M shells).

At about 06:54:00, Juno enters the polar auroral region where (1) upward electron beams (>30 keV) are observed (see also Mauk, Haggerty, Paranicas, Clark, Kollmann, Rymer, Mitchell et al. (2017)) and (2) the <30 keV electron intensities are very low.

The white pixels in panels (a), (b), (e), (f), and (g) after 06:54:00 are the result of low signal-to-noise ratios or no discernable counts above the background. It happens when the JADE background removal leaves many pixels empty of counts, which can be a sign of very low intensities or high penetrating background or both. Note that penetrating electrons also affect the JEDI data, particularly as the spacecraft flies in the horns of the radiation belts just preceding the time on the left of the plot (see other broader plot for the PJ1 time period in Mauk, Haggerty, Paranicas, Clark, Kollmann, Rymer, Mitchell et al. (2017)). JEDI has "witness" detectors that give a qualitative sense, but not a quantitative subtraction value, of the occurrence of penetrating electrons. Thus, it is likely that the energy flux in the first few minutes of this interval is overestimated due to penetrating radiation (see also Gérard et al., 2019). That would explain why the UV emissions stay dim while the total downward energy flux increases toward lower absolute latitudes.

The periodic pattern around 90° pitch angle, mostly visible in the lower energies but still visible in the highest energy range in panel (d), is due to spacecraft shadowing. The gyroradius of electrons in the strong

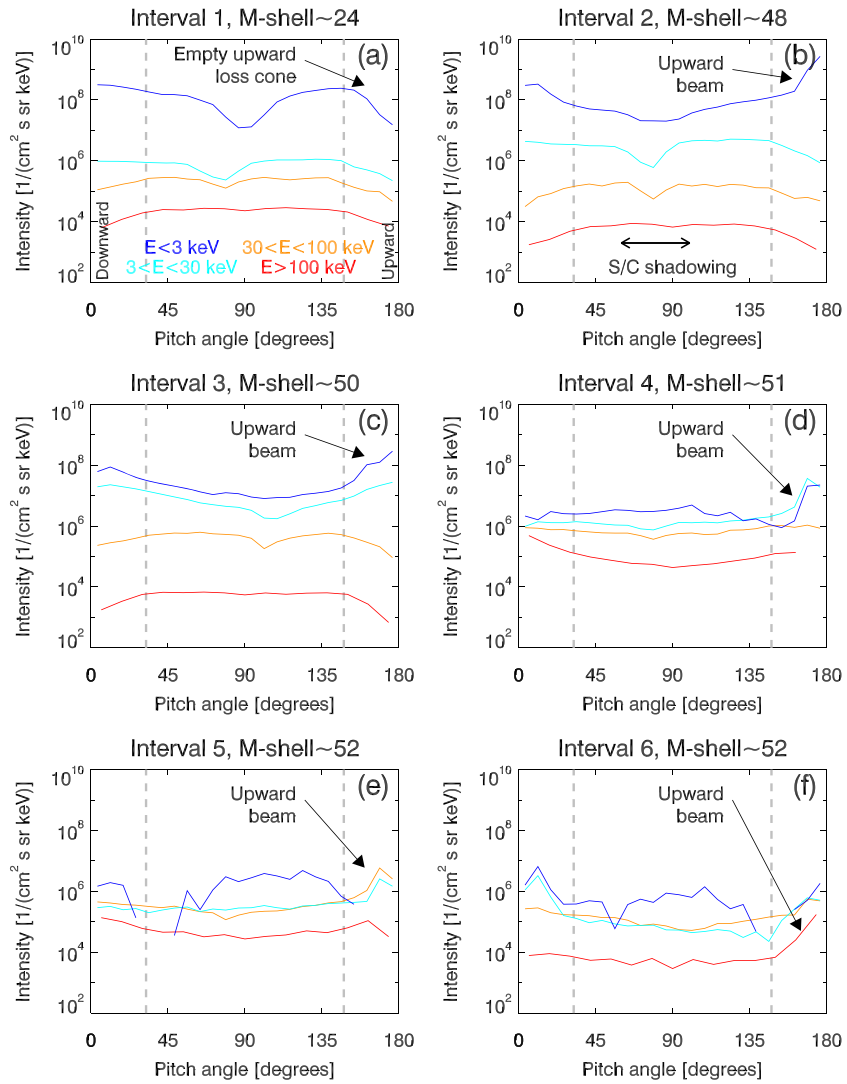


Figure 3. Pitch angle distributions for the six time intervals delimited in Figure 1 and Table 1. Electrons with pitch angles less than 90° move toward Jupiter (downward), and those with pitch angle more than 90° more away from Jupiter (upward). The vertical dashed lines show the average loss cone angle for the interval in Figure 1. Following the time sequence, a clear empty upward loss cone is visible in the lowest energies (0.1 to 3 keV) in (a). It is replaced by an upward electron beam in (b) and (c). Panels (d, e, and f) show more upward beams that increase in energy as the absolute latitude and M shell increase. The “dip” near pitch angles of $\sim 90^\circ$ is due to spacecraft shadowing (see text), affecting primarily the low-energy electrons.

magnetic field (~ 1.27 to 0.90 gauss for this interval) is comparable to the spacecraft dimensions (e.g., ~ 82 cm for 1 keV in a 1.27 gauss field). The near 90° pitch angle trajectories and low-energy electrons are the most affected by this shadowing (Allegrini et al., 2017). Another study to correct for this effect is ongoing but is not sufficiently mature to be incorporated in this study. However, that does not affect this study since the focus is on the electrons within the loss cones, which are much less, if at all, affected by the shadowing.

In Figures 1d–1g, we identified six time intervals, some of which include electron beams. The upward electron beams are visible in the lower energies at lower (absolute) latitudes (M shells) first, and then, as Juno moves toward higher (absolute) latitudes, they are progressively seen at higher energies all the way to above 100 keV in the polar region. Downward beams are also observed, although less frequently than the upward beams. Figures 3 and 4 illustrate this progression by showing the pitch angle distributions and the energy spectra for these time intervals. Table 2 gives the time intervals with corresponding M shell, magnetic latitudes, and radial distances.

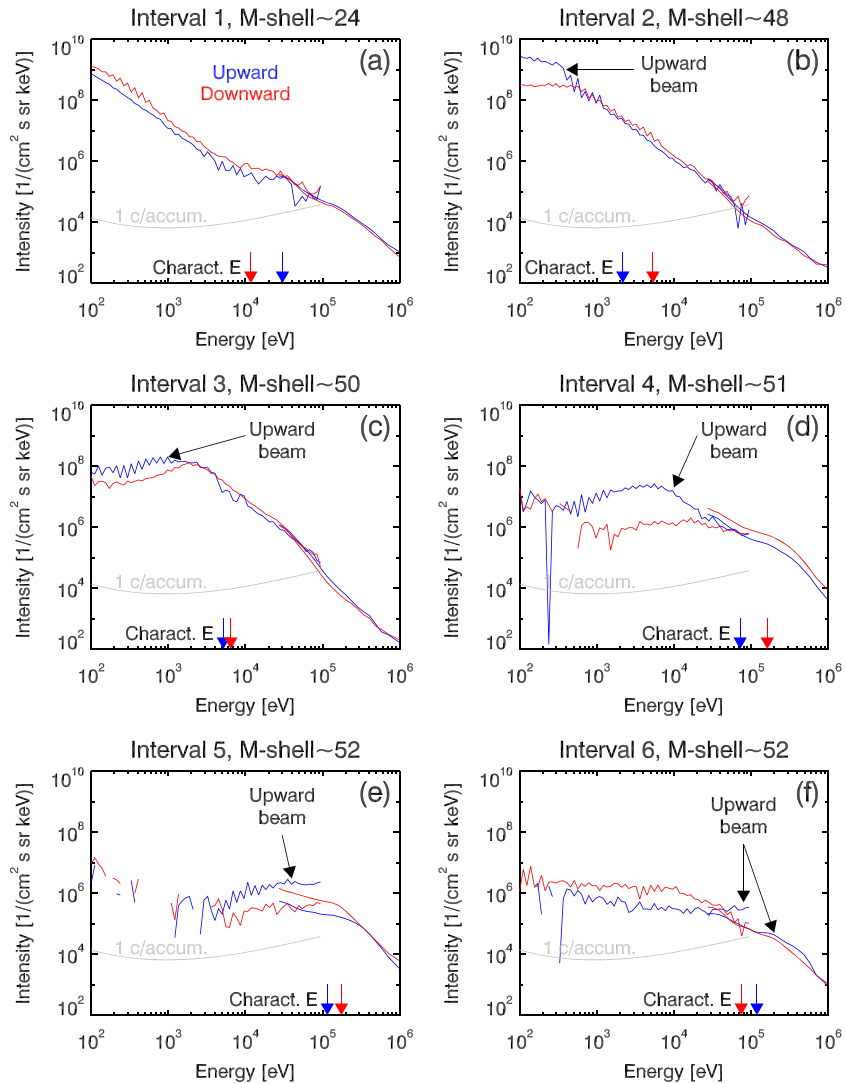


Figure 4. (a–f) Energy spectra of upward (blue) and downward (red) electrons within the loss cone for the six time intervals delimited in Figure 1 and Table 2. The high-energy portion ($\sim >100$ keV) only changes by about 1 order of magnitude over these time intervals, whereas the low-energy portion ($\sim <1$ keV) varies by more than 3 orders of magnitude. The arrows indicate the characteristic energies (equation 1). The light gray curves show the 1 count per accumulation level for JADE-E.

In Figure 3a for time interval 1 (*M* shell ~ 24), we see a clear empty upward loss cone in the lowest energy range (0.1 to 3 keV) and a full downward loss cone. The pitch angle distribution of 3- to 30-keV electrons is similar but with an upward loss cone somewhat less empty. The “dip” at pitch angles near 90° is the result of the spacecraft shadowing mentioned above. The highest energies (>30 keV) have a so-called pancake distribution. In Figures 3b and 3c near *M* shell ~ 48 to 50, the empty loss cone is replaced by a strong upward electron beam at the lowest energies. Further, Figures 3d–3f show the upward beams moving to higher energies as the *M* shell and latitude increase. Past *M* shell ~ 52 , the upward beams are only seen at energies greater than 30 keV.

Of particular interest, the pitch angle distributions of >30 -keV electrons transition from pancake distributions until interval 3 to uniform distributions (or slightly field aligned) from interval 4. Intervals 1, 2, and 3 are equatorward of the main oval, while 4, 5, and 6 are near or during the main oval crossing. The distribution differences could come from different acceleration mechanisms.

Table 2

Time Intervals Selected in Figure 1 and for Figures 3 and 4 With Corresponding M Shells, Magnetic Latitudes of Field Lines Projected at 400 km Above the 1-Bar Level, and Radial Distance

UTC time range on 2017-139	M shell (R_J) (JRM09+CAN1981)	Mag. lat. at 400 km ($^\circ$)	Distance (R_J)
06:49:12 to 18	24.4	-82.6	1.86
06:50:42 to 48	47.7	-83.6	1.90
06:51:28 to 34	50.2	-84.0	1.92
06:53:10 to 16	51.0	-85.0	1.96
06:53:44 to 50	51.5	-85.3	1.98
06:54:00 to 06	51.8	-85.4	1.98

Figure 4a shows the energy spectra of downward and upward electrons in the region where there is a clear empty upward loss cone in the lowest energies (<3 keV). The spectra are essentially power laws with an index of roughly -1.9 . Figures 4b–4f illustrate the change in energy of the upward beams, starting from 0.1 keV up to hundreds of keV. While the intensity of the higher energies varies by about an order of magnitude, that of the lower energies (<1 keV) varies by up to 3 orders of magnitude. The characteristic energy for the upward and the downward electrons is indicated with the arrows in each panel. The thin gray line shows the intensity equivalent to one count per accumulation for JADE.

At this point, it is interesting to compare these observations with what is known at Saturn. The electron distributions that cause the aurora at Saturn present remarkable similarities. Saur et al. (2006) reported measurements from the Low-Energy Magnetospheric Measurement System onboard the Cassini spacecraft. They found bidirectional electron angle beams in the equatorial region that statistically map into regions of Saturn's main aurora. The beams at Saturn are accelerated antiplanetward, similar to the upward beams described in Figures 1, 3, and 4. At Saturn, the beams are measured over the entire instrument energy range from 20 to 800 keV. At Jupiter, the upward beams are also measured from ~ 50 eV up to 1,000 keV. At Saturn, their energy distributions follow power laws with spectral index in the range from -1.6 to -2.6 , while at Jupiter the spectral index is about -1.9 for PJ6S (Figure 4b). Moreover, the energy flux of the beams increases by a factor of 10 at the lowest energies when Cassini is moving radially inward which is similar to what we see in Figure 4 where the intensities at low energies also increase by up to 3 orders of magnitude as we move toward lower M shells.

In addition to the main oval, Saturn's aurora also has a dimmer emission equatorward of the main oval called the outer emission. The outer emission boundaries map to a distance of ~ 6 – $7 R_S$ in the magnetic equatorial plane (Bader et al., 2020) corresponding to a striking plasma boundary at $7 R_S$ as identified in Schippers et al. (2008). Inward of that boundary, the electron pitch angle distributions are trapped and have pancake or butterfly distributions, whereas outward of that boundary, the pitch angle distributions are bidirectional. As a comparison with Jupiter, we use the pitch angle distributions in Figure 4. Panels (a) and (b) represent distributions equatorward of the main oval. They are pancake distributions for energies greater than 30 keV. As Juno gets closer to the main oval, the distributions tend to be more field aligned. Thus, there seem to be similarities between electron distributions at Saturn and Jupiter as well.

3.2. Energy Flux and Characteristic Energy

Continuing with the same interval as in Figure 1, we examine the energy flux and characteristic energy of the electrons in Figure 5. The top two panels show energy time spectrograms of the energy flux for upward (a) and downward (b) electrons. The black curve is the characteristic energy of the electrons. Panel (c) shows the upward (blue) and downward (red) total energy flux, and the UV brightness shifted by 21 s (same as Figure 1c). Panels (d) and (e) show the fractional contribution to the total energy flux of 0.1- to 3-keV (blue), 3- to 30-keV (cyan), 30- to 100-keV (orange), and 100- to 780-keV (red) electrons. Note that in these panels the sum of the four contributions (or fractions) adds up to 1.0 for every time step. Panel (d) represents upward fluxes, and panel (e) represents downward fluxes, both for pitch angles within the upward or downward loss cone.

The 100- to 780-keV electrons contribute up to ~ 70 – 80% of the total downward energy flux for most of the time interval and during the main oval crossing. However, there is a region equatorward of the main oval where the 3- to 30-keV electrons provide the dominant contribution to the total energy flux: The largest contribution (at $\sim 40\%$) happens at 06:51:45. The gray vertical lines in panels (d) and (e) delimit the times of the “peak” of the 3- to 30-keV electron fraction contribution. These limits were determined manually using Figures 5 and S7 to S21e with a resolution of 15 s. They correspond to the beginning and the end of where the 3- to 30-keV energy flux peaks. The times are listed in Table 1 Columns 9 and 10.

The characteristic energy (black curve panels (a) and (b)) is above 100 keV during the main oval crossing ($\sim 06:52:45$ to $\sim 06:54:00$) and in the polar region (after $\sim 06:54$). It is below 30 keV equatorward of the main

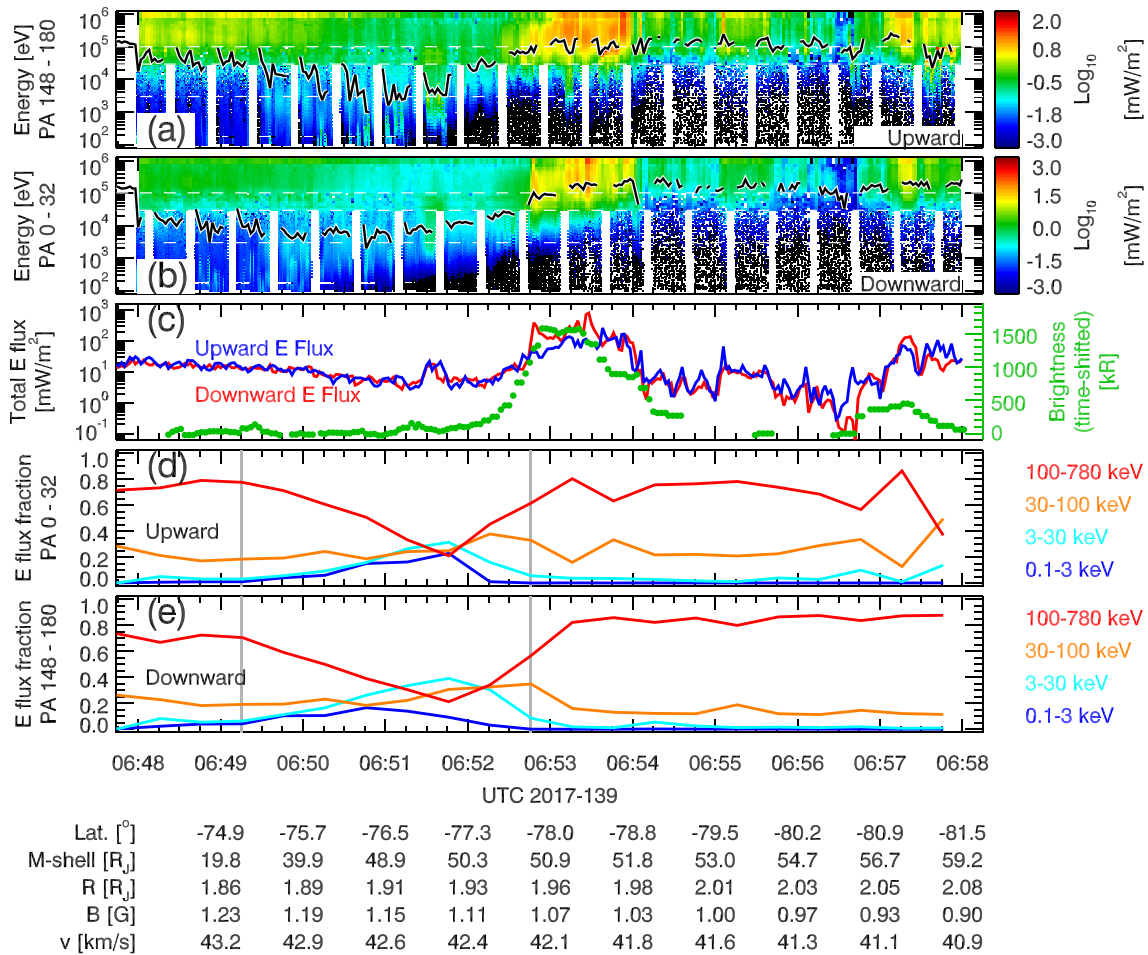


Figure 5. The top two panels show the combined JADE and JEDI energy fluxes for upward (a) and downward (b) electrons during the main auroral oval crossing in the south from Perijove 6 (same time interval as Figure 1). The black curves are the characteristic energy. Panel (c) shows the total energy flux within the loss cone of upward and downward electrons, as well as the UV brightness shifted by 21 s (same as in Figure 1c). The bottom two panels show the fraction of the energy flux in the energy bands listed on the right with respect to the total energy flux for upward (d) and downward (e) electrons within the loss cone. The 100- to 780-keV electrons provide the largest contribution to the total energy flux for most of the interval, except for a region just equatorward of the main oval crossing where the 3- to 30-keV electrons dominate for a short duration (<1 min). The gray vertical lines delimit the “peak” of the 3- to 30-keV electron fraction contribution (see also Table 1). The *M* shell values are derived from JRM09+CAN1981.

oval crossing. The lowest value of the characteristic energy of the downward electrons (<3 keV) also falls in the interval where the 3- to 30-keV electron energy flux peaks.

We make similar observations (i.e., peak of 3- to 30-keV energy flux contribution and lowest characteristic energy equatorward of main oval) for the other perijove passes of this study (see Figures S7 to S21 in the supporting information). In about half the passes the 3- to 30-keV electrons provide the dominant contribution to the total energy flux at their peak. We list the times that delimit the peaks in Columns 9 and 10 of Table 1, as well as corresponding radial distances (Column 11 and 12) and *M* shells (Columns 13 and 14).

The existence of the region where the 3- to 30-keV electron energy flux peaks and where the characteristic energy is lowest (<10 keV, sometimes as low as 1 keV) is a recurring feature of the electron observations in the auroral regions. Moreover, when the brightness curve shows a peak that is reasonably well correlated with the peak of the downward electron energy flux (e.g., PJ3S, PJ4S, PJ5N, PJ6N, and PJ6S), then this region is adjacent to the main oval crossing and equatorward of it. Based on the consistency of these observations, we postulate that the polarward edge of the region where the 3- to 30-keV electron energy flux peaks corresponds to the equatorward edge of the main oval. If that is the case, then it is a useful metric to place the electron observations into the context of the main emissions. It provides an “anchor” to relate the electron observations to the main oval.

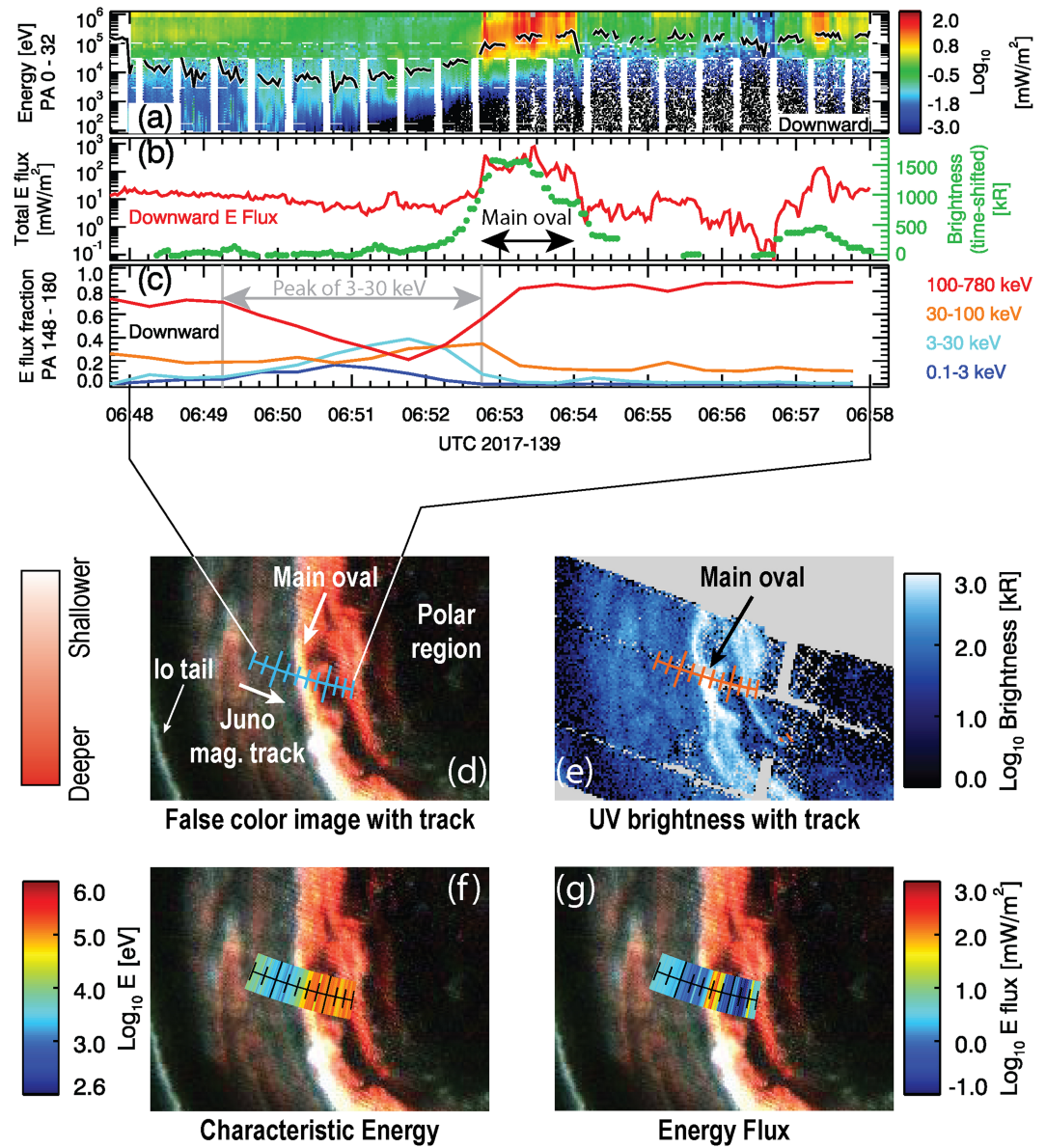


Figure 6. (a) Downward electron energy flux as a function of energy and time with characteristic energy (black curve) for the same time interval as Figure 1 (PJ6S). (b) Total downward energy flux (red) and UV brightness (black, shifted by 21 s; see Figure 1c). (c) Fraction of the energy flux in the energy bands listed on the right with respect to the total downward energy flux. The gray vertical lines bound the “peak” of the 3- to 30-keV electron fraction contribution (see also Table 1). (d) False color image from UVS with Juno’s magnetic footprint track. The tick marks are 1 min apart and start at 06:48. (e) UV brightness image from UVS with track. (f) Characteristic energy projected onto the track and the false color image. (g) Downward energy flux projected onto the track and the false color image.

The equatorward edge of the region is at an average M shell of ~ 20 with a standard deviation of 7. Interestingly, the polarward edge of the region characterized with the peak of the 3- to 30-keV electron contribution consistently maps to M shells of ~ 50 – $53 R_J$ with a few exceptions (average of 51.2 with a standard deviation of 0.8). This means that the mapping from JRM09+CAN1981 places the main oval to M shells greater than 50. That obviously contradicts the general picture where the main oval is the result of the breakdown of corotation of Jupiter’s plasma disk (Cowley & Bunce, 2001; Hill, 2001) which is predicted to occur at radial distances of ~ 20 – $30 R_J$. It is likely that an improved M shell mapping based on a refined plasma disk model will resolve this issue.

Figure 6 illustrates how the electron energy flux and characteristic energy relate to the UV emissions in a graphical way. Panels (a)–(c) are the same as Figures 5b, 5c, and 5e focusing only on the downward electrons. Panel (d) shows Juno's magnetic footprint track for the time interval of panels (a)–(c) projected onto a reconstructed false color image from UVS. The tick marks on the track are 1 min apart. Juno's footprint is moving polarward (to the right). The main oval is the bright white arc crossed between ~06:52:45 and ~06:54:00. The false color image is the result of frames collected over a period of 1 hr (from 06:40 to 07:40). The wavelength of the emission is used to determine these false colors. The shorter wavelengths are partly absorbed by the methane column density, whereas the longer wavelengths are less affected. Thus, the red color here indicates emissions created by higher-energy electrons that penetrate deeper inside Jupiter's atmosphere, and the white color comes from emissions higher in the atmosphere.

Panel (e) shows the UV brightness from frames collected from 06:45 to 06:58 very close in time to when the electron measurements were taken. The average time difference between when the frames were collected and when Juno was magnetically connected to that region is less than 2 min. Panels (f) and (g) show the characteristic energy and the energy flux of downward electrons projected onto the false color images.

There is good qualitative agreement between the high characteristic energies and the reddish color of the false color image. This is expected since higher-energy electrons will penetrate deeper into Jupiter's atmosphere and create emission from lower altitudes. Similarly, the fainter white emissions from equatorward of the main oval correspond to lower characteristic energies. The peak energy flux lines up with the main oval crossing as expected from panel (b).

Figure 7 shows the characteristic energy and the energy flux of downward electrons projected onto the reconstructed, false color UV images for the first eight science perijoves roughly uniformly distributed in System III longitude. Each pass is projected onto the corresponding false color image that was acquired for 40 to 60 min around the actual crossing of the main oval.

The north pole projections are on the left and the south on the right. The bottom set of false color images is bare images with only the tracks. The region where the bars of the characteristic energy and the energy flux are narrower and the blue boxes in the bottom row correspond to the time intervals listed in Columns 9 and 10 of Table 1, where we identified the peak of the 3- to 30-keV electrons in the energy flux fraction contribution. This region is usually of fainter emission and, again, situated adjacent to and equatorward of the main oval when the oval is clearly discernable. It is also the region where the characteristic energy is consistently lowest. Similarly to Figure 6f, there is good qualitative agreement between the red/white colors of the false color images and the characteristic energy. Higher characteristic energies in the polar region and sometimes at the low latitude end of the intervals correspond to reddish colors, whereas the lower energies correspond to the white. The lower characteristic energy region for the downward electrons also corresponds to outer emissions (e.g., Dumont et al., 2014; Radioti et al., 2009), generally associated with pitch angle diffusion in the loss cone (Li et al., 2017).

While the characteristic energy has a consistent pattern for all perijoves, the energy flux does not show it as clearly. There is also quite a bit of variability from perijove to perijove. For example, PJ7 north shows some strong energy flux intervals on each side of the average main oval, while PJ3 north looks rather quiet in comparison. However, when the main oval consists of a single arc (e.g., PJ3S, PJ4S, PJ5N, PJ6N, and PJ6S), the energy flux peak seems to line up fairly well with the bright emission.

In Figure 8, we show the logarithm of the upward to downward energy flux ratio (capped to 1 in absolute value) projected onto the north and south poles. Blue corresponds to regions with net upward energy flux and red to the opposite. The false color UV images are shown underneath the tracks as well as the average main oval location from Bonfond et al. (2012), derived using pre-Juno observations from the HST.

Most of the time, the upward and downward energy fluxes are roughly the same (~74% of the time within a factor of 2 of each other). However, there generally seems to be more energy flux upward in the polar region and more downward energy flux equatorward of the main emission.

On the one hand, the excess of upward energy flux can be the result of (1) the upward electron beams significantly contributing to the energy flux, (2) flying above the acceleration region and measuring electrons that have been accelerated upward, and (3) a net downward current as would be expected in the polar region. On the other hand, the excess of downward energy flux can be the result of (1) a partially empty

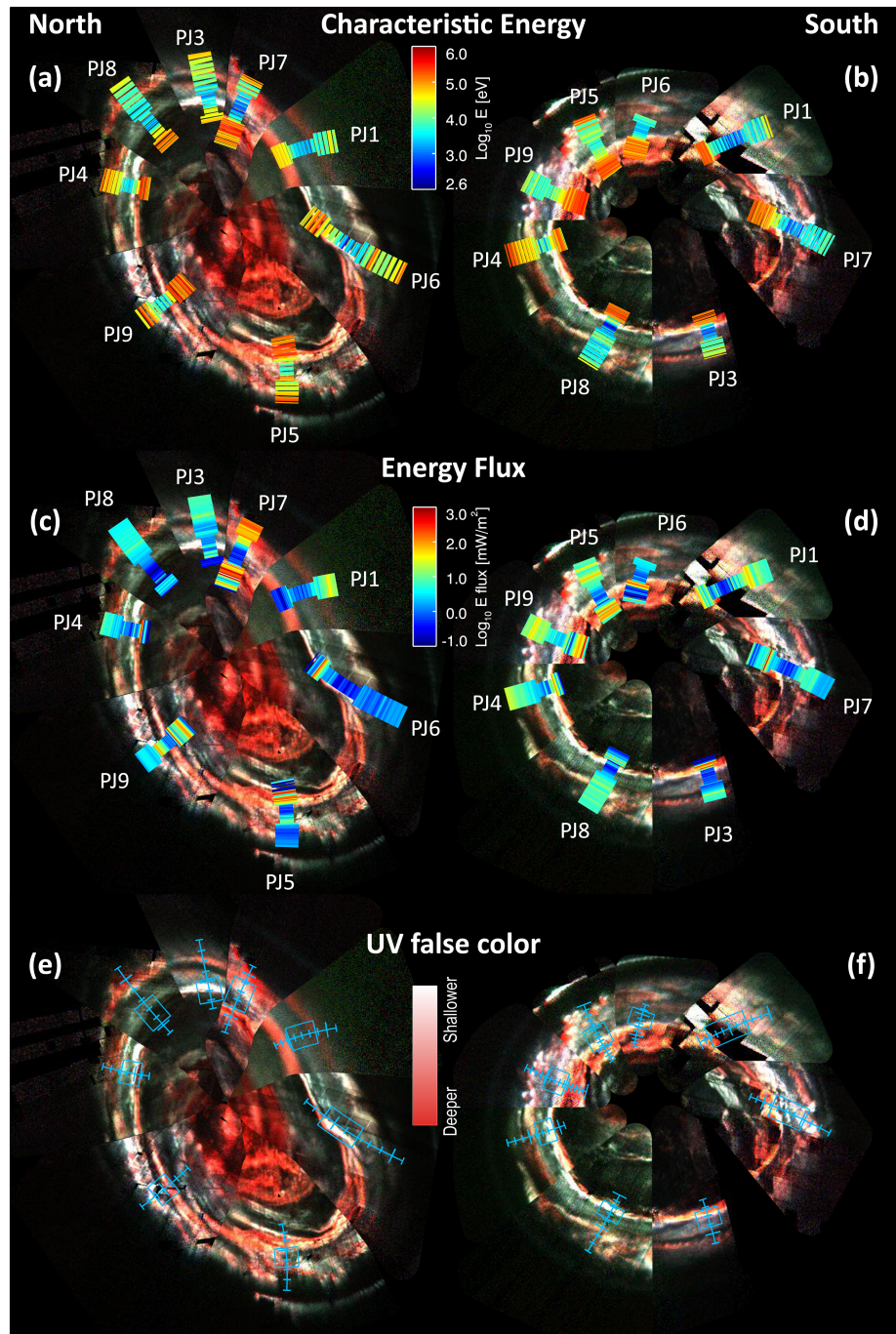


Figure 7. Characteristic energy (a) and (b) and energy flux (c) and (d) projected onto false color images of the north (left) and south (right). Panel (e) and (f) show the bare images with tracks. The false color images were collected for 40–60 min around the main oval crossing. There is a good agreement between the red (white) color of the images with the higher (lower) values of the characteristic energy. The area where the bars in panels (a)–(d) are narrower and where the boxes are shown in the bare images (e) and (f) corresponds to the region where the 3- to 30-keV electron energy flux contribution to the total energy flux peaks (see also Table 1 and Figures 5 and 6).

upward loss cone and full downward loss cone, (2) flying below the acceleration region and measuring downward accelerated electrons, and (3) a net upward current as would be expected equatorward of the main oval.

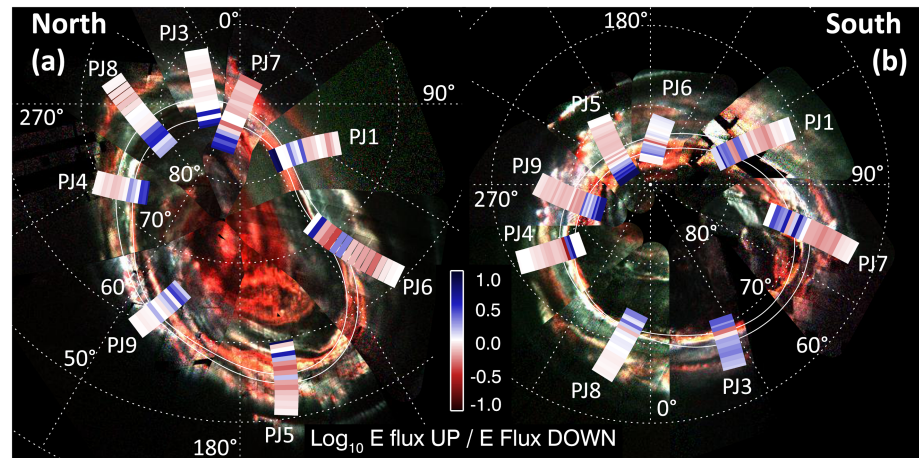


Figure 8. Ratio of the upward energy flux to the downward energy flux projected onto the north (a) and south (b) pole. We also show the average oval location from Bonfond et al. (2012).

Figures 9 and 10 show the logarithm of the upward to downward energy flux ratio as a function of M shell as determined using JRM09 and a current sheet model for all perijove passes for the north and south, respectively. The black symbols correspond to the times of the peak of the 3- to 30-keV electron energy flux (also shown with the shaded areas). The orange (blue) symbols are for observations equatorward (polarward) of that region.

As was already mentioned earlier, the polarward edge of the 3- to 30-keV peak is consistently around M shell of ~ 50 (using JRM09+CAN1981). This boundary, which we believe is where the equatorward edge of the main oval is, also seems to align with a change in the energy flux ratio. With the exception of PJ5 and PJ9 in the north and PJ3, PJ5, PJ6, and PJ9 in the south, the upward to downward energy flux increases at the boundary when going to higher M shells. But in most cases, there seems to be a clear change, maybe even a discontinuity, in this ratio around M shell of 50. This boundary also corresponds to where magnetic field perturbations are observed due to an upward field-aligned current (Kotsiaros et al., 2019).

At the equatorward M shell edge of the 3- to 30-keV peak interval, the ratios are similar to what they are in the interval and there is no change or discontinuity. The scatter of the orange symbols in Figure 9h at the lower M shells is probably due to low signal-to-noise ratio in a region where there is penetrating radiation (see Figure S20 in the supporting information).

Figures 11 and 12 show the total downward energy flux as a function of the characteristic energy for the north and south, respectively. The color of the symbols follows the same scheme as for Figures 9 and 10. The black symbols correspond to the 3- to 30-keV energy flux peak intervals, and the orange (blue) symbols are equatorward (polarward) of those intervals. Clark et al. (2018) showed similar results for >30 -keV electrons. This study includes lower-energy electrons (down to ~ 50 eV). Figures 11 and 12 illustrate how different the conditions are from one perijove pass to another. They also show that there are large variations (for both the energy flux and the characteristic energy) even during a single perijove pass (e.g., PJ7 north or PJ1 south). In some cases, for example, in PJ3 and PJ4, there is a qualitatively good correlation between the two quantities for the black and orange symbols.

There does not seem to be a clear trend common to all perijove passes. The black and orange symbols seem to follow similar trends for PJ3N, PJ4N, PJ4S, PJ6S, and PJ7S but not so for the other passes. The blue symbols (main oval and polar region) cover a large energy flux range, while their characteristic energy is usually around 100 keV and above. It seems that the blue and black symbols land on different parts of this parameter space which could point to different energization mechanisms.

The lowest measured characteristic energy can be below 1 keV (e.g., PJ8 south). Characteristic energies below a few tens of keV are found only equatorward of the main oval (black and orange symbols).

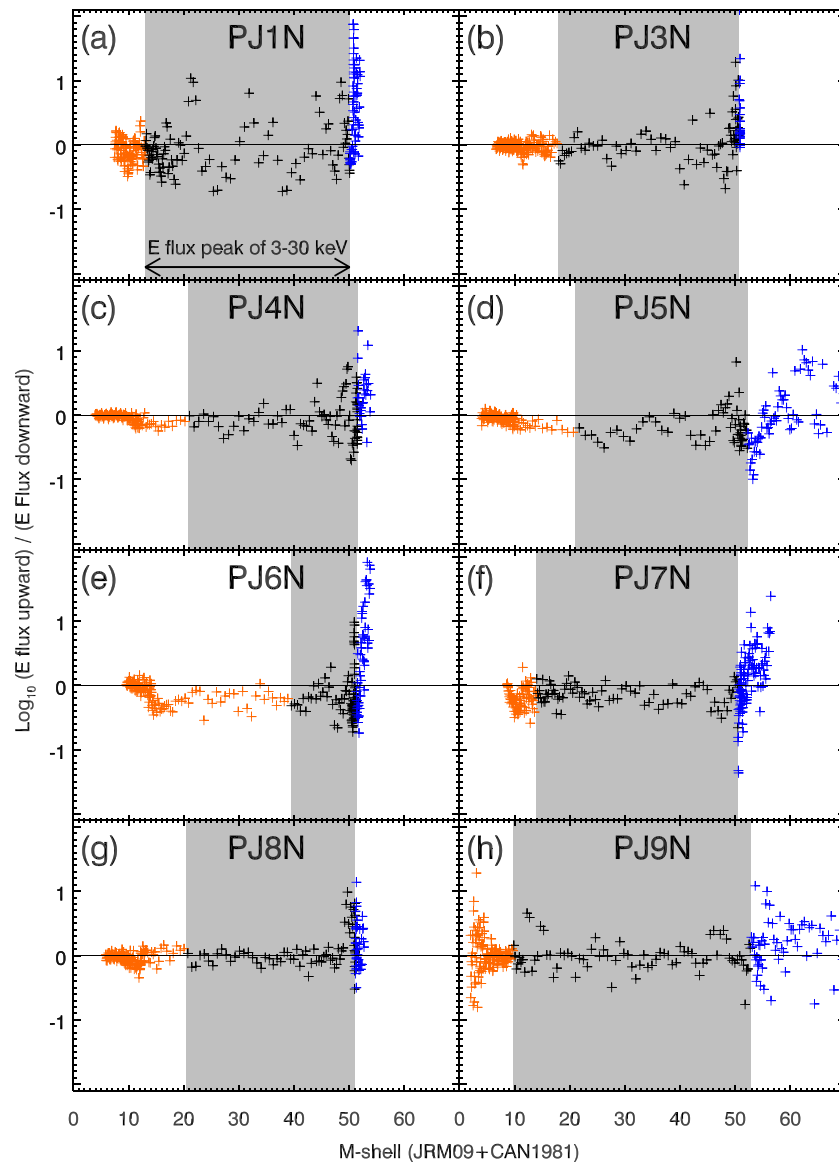


Figure 9. (a–h) Logarithm of the energy flux ratio (upward/downward for electrons in the loss cone) for PJ1 to PJ9 North as a function of M shell for the time intervals of this study. The gray range corresponds to that of the peak in energy flux of the 3- to 30-keV electrons. The symbols for M shells polarward of that range are in blue and equatorward in orange. For most of the passes (except PJ9), there seems to be a sharp transition at the polarward edge of the shaded area. From Figure 5 (and other figures in the supporting information), that transition corresponds to the equatorward edge of the main oval. See also Figure 10 for the South passes.

The UV brightness of the aurora is related to the energy deposited into the atmosphere. Based on several aeronomic models, Gustin et al. (2012) proposed a value of $10 \text{ kR}/(\text{mW}/\text{m}^2)$ as a rule of thumb for electrons in the 70- to 140-keV range. Here, we can test this relationship using the UV and electron data.

When comparing the UV brightness with the total downward energy flux for the different passes, we find five passes (PJ3S, PJ4S, PJ5N, PJ6N, and PJ6S) where the peak brightness at Juno’s magnetic foot point and the peak electron energy flux coincide. The UV images for these five passes show distinct features with corresponding variations in brightness that are easily correlated with the electron energy flux. That allows us to align the two data sets similar to what has been done with the 21-s shift of the UV brightness for PJ6 south (Figure 1). The time shifts are likely due to small errors in the model-dependent mapping of Juno’s foot point. The other passes of this study have less distinct features and more complicated structures which

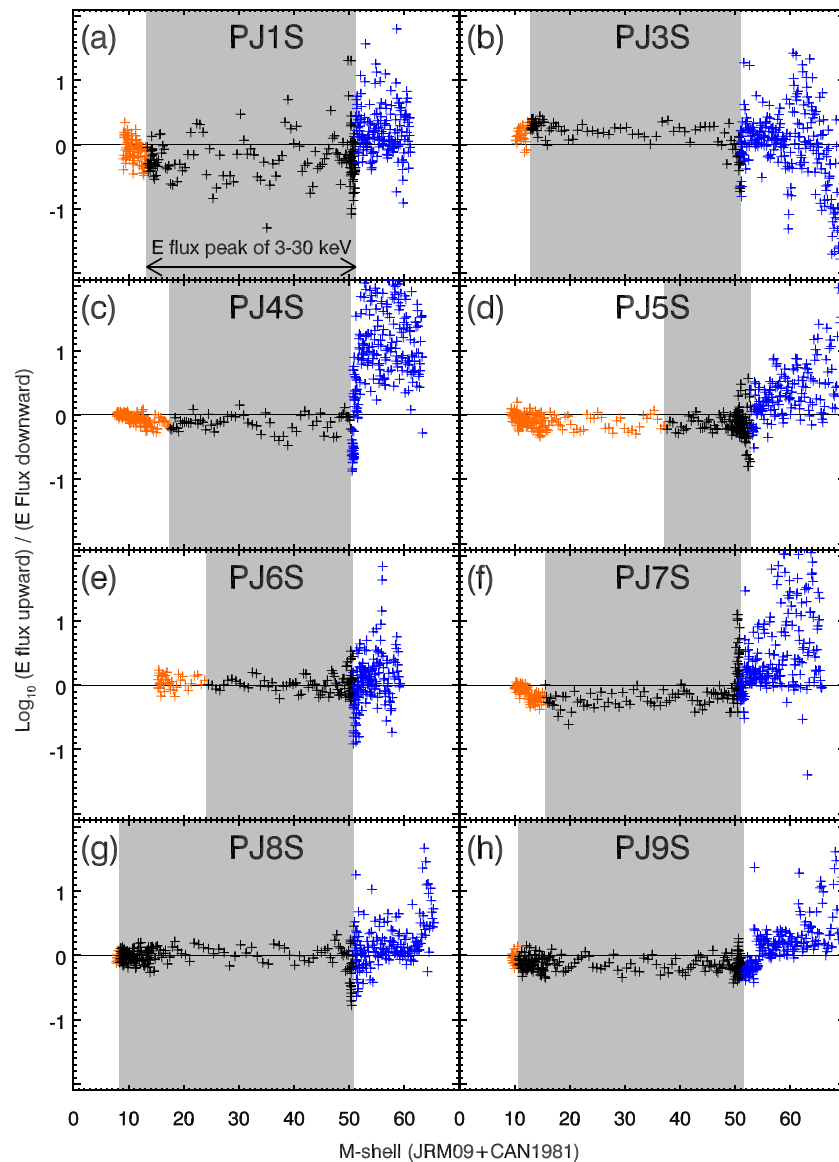


Figure 10. Same as Figure 9 but for the South passes.

make it difficult to reliably align the data sets. Moreover, some passes have large time differences (>20 min) between the time when the electron measurements were made and when the UV images were acquired. Thus, we focus only on the five passes that present the best correlation among all the perijoves discussed in this study.

To determine the time shift to apply to the derived UV brightness, we repeat the same process as was done for PJ6S (see Figure 1). In short, we maximize the Spearman's rank correlation between the UV brightness and the total downward energy flux by varying the time shifts of the UV brightness data. The correlation coefficients range from a minimum of ~ 0.79 to a maximum ~ 0.87 , and the time shifts range from 8 to 24 s.

Using the Grodent et al. (2001) atmosphere model, Gustin et al. (2016) determined that the UV intensity depends on the mean energy of the electrons (their Figure 12d) for the main emission. We plot the data from the five passes in the same format in Figure 13, that is, the UV brightness per incident energy flux as a function of characteristic energy. We also show the curve from Gustin et al. (2016). In Figure 13a we only use the data points when the brightness is more than 10% of the maximum brightness (i.e., we select the data points of the brightest 90%) during the interval of the pass. Figure 13b is the same with only the brightest 66% data

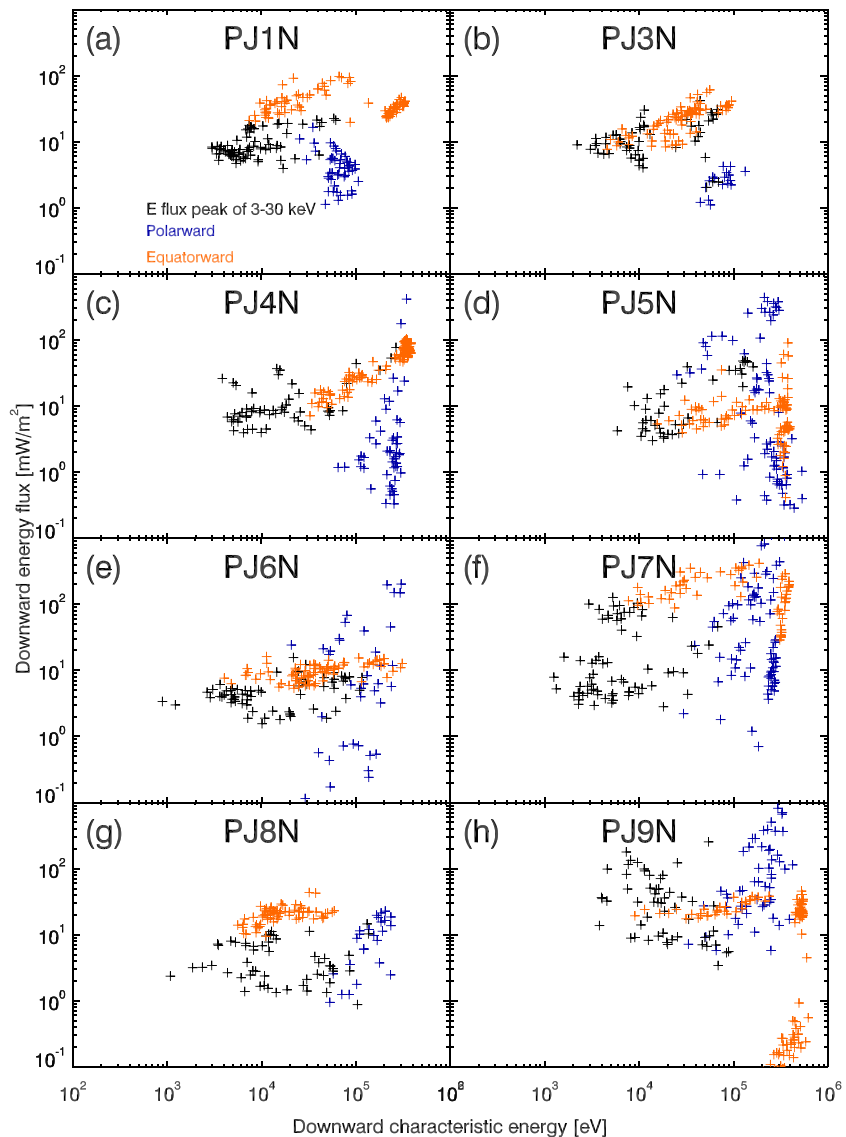


Figure 11. (a–h) Total downward energy flux as a function of downward characteristic energy in the north. The colors correspond to different time intervals: Black is for a time interval when the energy flux contribution from 3- to 30-keV electrons peaks (see Figures 5 and S7 to S21); blue (orange) is for times when Juno is polarward (equatorward) of that interval. The black data points also correspond to the minimum of the characteristic energy.

points. The dark red diamond symbols are the 20-point medians. The vertical “error” bars comprise 50% of the data points, and the horizontal error bars represent the energy span of the 20 data points.

The agreement between the medians and the curve is good for energies of more than about 50 keV, and the trend is consistent. The scatter of the data at lower energies (<~30 keV) is significant which makes it hard to draw clear conclusions. Nevertheless, it seems that the conversion from energy flux to UV brightness for lower-energy (<30 keV) electrons is more efficient than the model suggests. The proposed value of 10 kR/(mW/m²) for electrons in the 70-to 140-keV range is consistent with our results.

One might question whether limiting the analysis from Figure 13 to a subset of the perijove passes would invalidate the results. We can think of a number of reasons that can explain differences between the expectations from the downward electron energy flux and the observations of the UV brightness along the magnetic track.

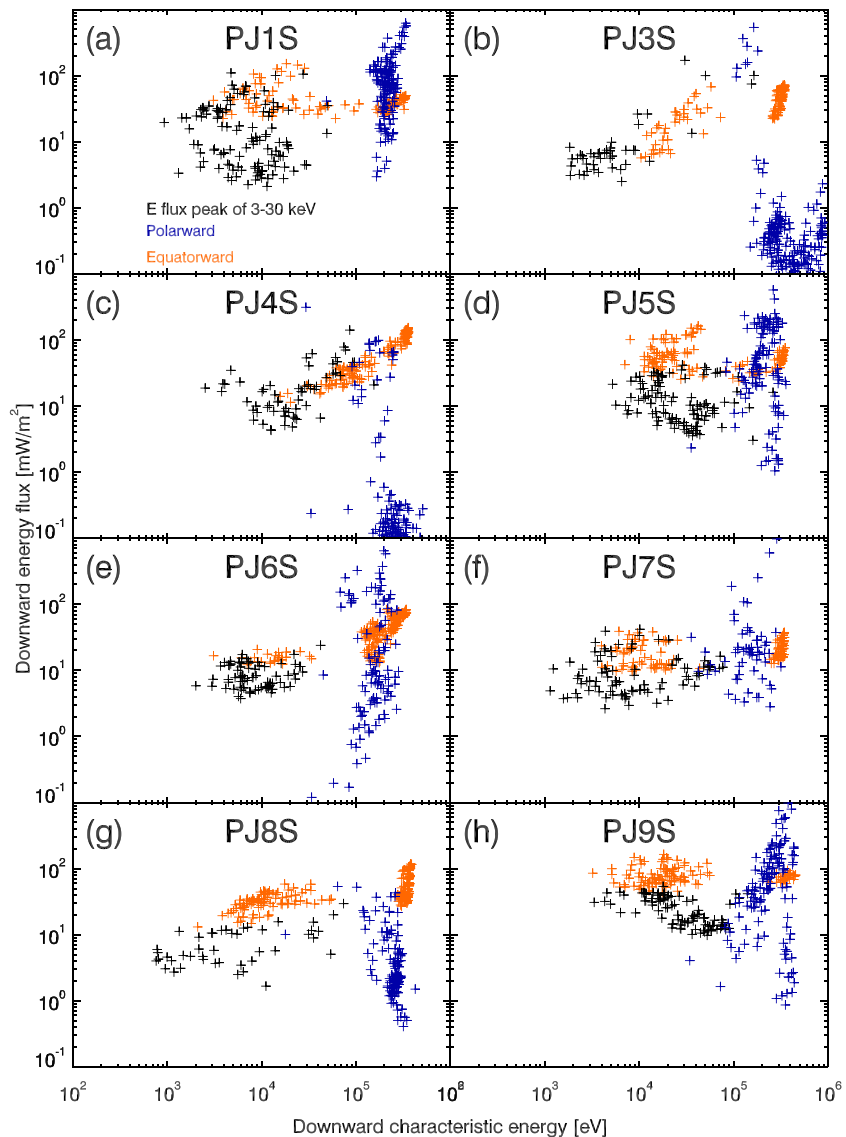


Figure 12. Same as Figure 11 but for the south.

The FOVs of the JADE and JEDI instruments are different and do not always have full pitch angle coverage. Narrow (in pitch angle) field-aligned beams could be missed. For example, JADE repeatedly measures short time (~ 1 s or less) scale structures (e.g., beams) over the auroral region (Allegrini et al., 2017). Thus, it is not impossible that sometimes such structures may fall outside the JADE and JEDI FOVs. In fact, we show in the supporting information (Figure S6) that there are instances when JADE measures an electron beam that is outside JEDI's FOV, and vice versa. Therefore, JADE and/or JEDI could sometimes only sample a fraction of the precipitating electron population and thus would underestimate the total energy flux.

The UV brightness at Juno's magnetic foot point is derived using an average over a 0.1° radius circle, which corresponds to a spot of about 50 to 270 km for the range of distances for this study. If the spot is larger than the UV feature, then the calculated brightness is underestimated since it is averaged over the entire spot. If structures in the electron data are of the order of 1 s or less and the spacecraft moves at a speed of 40–50 km/s, then UV features smaller than the spot size are plausible.

We also mentioned that the magnetic mapping, even though much improved over previous models, still has some uncertainty to it. While a shift along the track translates into a time shift of the UV data set, a lateral

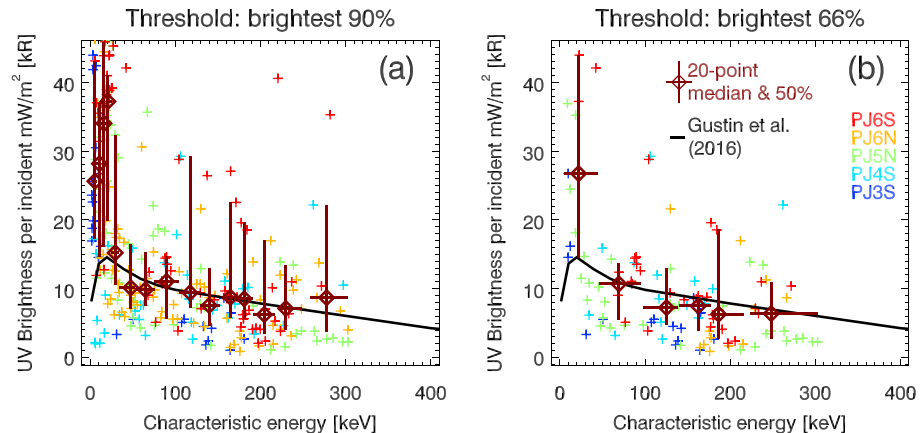


Figure 13. UV brightness divided by electron energy flux as a function of the electron characteristic energy. Panel (a) is using data points when the brightness is between 10% and 100% of the maximum brightness during the interval, and panel (b) is using data points when the brightness is in the upper 66% of the maximum. The “plus” symbols are color coded according to the different passes indicated in panel (b). The dark red diamonds are 20-point medians. The vertical bars represent 50% of the data points, and the horizontal bars represent the energy span of each group of 20 data points. The black curve is a prediction from Gustin et al. (2016).

shift can easily change the derived brightness by pointing to a different feature. Quantifying the mapping error is not an easy task, and it is not part of this study. What we can do, however, is to look at differences in the mapping from different magnetic field models. Using a time when Juno is crossing the main oval for each perijove, we look at the separation between the footprints using JRM09 and two other magnetic field models: Voyager Io Pioneer 4 (VIP4; Connerney et al., 1998) and VIP Anomaly Longitude (VIPAL; Hess et al., 2011). The differences between the footprint locations range from ~380 up to ~5,800 km. While the distance between the footprints obtained from the different models is not necessarily a good proxy for the mapping accuracy, it supports the idea that the spot size might probably be smaller than the mapping error. Thus, the measured electron distribution may not always correspond to the feature that is mapped. Note also that the time shifts derived above can be used to estimate potential mapping error along the track. For example, the 21-s shift for PJ6S (Figure 1) translates into a ~237-km shift along the track.

Finally, note that other studies by Ebert et al. (2019) and Gérard et al. (2019) find times when the energy flux is correlated with the UV brightness at the magnetic foot point of Juno and also other times when it does not, probably for similar reasons.

4. Summary and Discussion

We presented the first comprehensive evaluation of Jovian auroral electron characteristics over the entire relevant range of energies and provided context from UV observations taken over the main auroral emissions during the first eight science perijoves from Juno. It has been anticipated from pre-Juno measurements that Jupiter’s main aurora is generated predominantly by precipitating electrons with energies in the tens of keV range but often extending up to characteristic energies as high as 500 keV, and indeed, such regions are observed by Juno. We summarize our findings here:

1. In the main auroral region, electron energy spectra are mostly broadband distributions or power laws. Earth’s analog “inverted Vs” have been observed with Juno (e.g., Mauk et al., 2018), but they are far less frequent than the broadband distributions. Low-energy electrons (<1 keV) show large intensity differences (~3 orders of magnitude) between the low (~75°) and the high (~80°) latitudes of the main emissions. On the contrary, higher-energy electrons (>100 keV) show smaller intensity differences (<1 order of magnitude) over the same range.
2. Spatially narrow and/or temporally short field-aligned electron beams are observed at all energies between 50 eV and 1 MeV (see also Allegrini et al., 2017; Mauk, Haggerty, Paranicas, Clark,

- Kollmann, Rymer, Mitchell et al. (2017)). Upward (moving away from Jupiter) beams of higher energies are observed at higher latitudes and in particular in the polar auroral region. Lower-energy upward beams are observed at lower latitudes. Downward beams are also observed but less frequently than upward beams.
3. A partially empty upward loss cone is observed equatorward of the main emission up to about 30 keV and possibly extending to all energies and latitudes. We interpret this as a “diffuse aurora” region where electrons in the downward loss cone strike the atmosphere and are lost, resulting in empty upward loss cones.
 4. There is a region that maps to emissions adjacent to and equatorward of the main auroral oval where (i) the energy flux of 3- to 30-keV precipitating electron peaks, (ii) the characteristic energy is below 10 keV with a minimum as low as 1 keV for PJ8 south, and (iii) the 3- to 30-keV energy flux even dominates the >100-keV energy flux for ~30% of the passes from PJ1 to PJ9. Outside that region, the >100-keV electrons contribute to most (>~70–80%) of the total downward energy flux and the characteristic energy is usually around 100 keV or higher. This pattern is a recurring feature of the electron observations in the auroral regions. We postulate that the poleward edge of the region where the 3- to 30-keV electron energy flux peaks corresponds to the equatorward edge of the main oval. Using the JRM09 magnetic field model with a current sheet model (Connerney et al., 1981, 2018), the boundary is mapped at M shells of 51.2 ± 0.8 . A refined current sheet model will likely bring this boundary closer to the expected 20–30 R_J .
 5. The upward and downward electron energy fluxes are within a factor of 2 of each other for 74% of the time. However, there generally seems to be more energy flux upward in the polar region and more downward energy flux equatorward of the main emission. Large variations of energy flux and characteristic energy are observed from pass to pass and even during a single pass.
 6. The rule of thumb for the conversion of energy flux to brightness ($\sim 10 \text{ kR}/(\text{mW}/\text{m}^2)$) for electrons in the 70- to 140-keV range is consistent with our results. There is a weak dependence between the UV brightness per mW/m^2 and the characteristic energy above ~50 keV. Our results also suggest that the conversion from energy flux to UV brightness for energies below ~30 keV is more efficient than the model prediction from Gustin et al. (2016).

The existence of the region where the 3- to 30-keV electron energy flux peaks just equatorward of the main oval is consistent for all passes. Therefore, this region is probably a signature of a large-scale structure that is likely important for understanding the general processes at play to create the aurora. Additional temporal and or spatial variations on top of this recurring feature are clearly seen and require case-by-case analyses.

The perijove passes for this study covered a local time range from about 18 (PJ1) to 15 (PJ9), which probably is too narrow to see trends with local time. Moreover, the crossings of the main emission are distributed in System III longitude by nature of Juno's orbit. However, we list the auroral family types according to Grodent et al. (2018) in Table 1 for reference for future studies. By the end of Juno's prime mission, the local time of the crossings will have decreased to about 9.4 (PJ34). An extended mission could bring the local time coverage to well past the dawnside into the nightside, which would provide unprecedented views of the aurora (because the nightside aurora is not visible from Earth) as well as corresponding electron distribution measurements.

The JADE sensitivity has been readjusted using in-flight cross calibration with the Waves investigation, and we recommend using the new sensitivity given in the supporting information material.

References

- Adriani, A., Filacchione, G., di Iorio, T., Turrini, D., Noschese, R., Cicchetti, A., et al. (2017). JIRAM, the Jovian infrared auroral mapper. *Space Science Reviews*, 213(1-4), 393–446. <https://doi.org/10.1007/s11214-014-0094-y>
- Allegrini, F., Bagenal, F., Bolton, S., Connerney, J., Clark, G., Ebert, R. W., et al. (2017). Electron beams and loss cones in the auroral regions of Jupiter. *Geophysical Research Letters*, 44, 7131–7139. <https://doi.org/10.1002/2017GL073180>
- Allegrini, F., Desai, M. I., Livi, R., Livi, S., McComas, D. J., & Randol, B. (2009). The entrance system laboratory prototype for an Advanced Mass and Ionic Charge Composition Experiment (AMICCE). *The Review of Scientific Instruments*, 80(10), 104.502. <https://doi.org/10.1063/1.3247906>
- Bader, A., Cowley, S. W. H., Badman, S. V., Ray, L. C., Kinrade, J., Palmaerts, B., & Pryor, W. R. (2020). The morphology of Saturn's aurorae observed during the Cassini Grand Finale. *Geophysical Research Letters*, 47. <https://doi.org/10.1029/2019GL085800>
- Bagenal, F., Adriani, A., Allegrini, F., Bolton, S. J., Bonfond, B., Bunce, E. J., et al. (2017). Magnetospheric science objectives of the Juno mission. *Space Science Reviews*, 213(1-4), 219–287. <https://doi.org/10.1007/s11214-014-0036-8>

Acknowledgments

We thank all the outstanding women and men who have made Juno and the instrument suite so successful. The authors would also like to thank the following individuals who have helped in different capacities: Chad Loeffler, Nigel Angold, Eric Fattig, Patrick Phelan, Greg Miller, Dave Cronk, Craig Pollock, Michelle Thomsen, George Hospodarsky, Denis Grodent, Maïté Dumont, Stavros Kotsiaros, Ali Sulaiman, Juan Muñoz, Thomas Kim, Lizeth Magana, Benjamin Byron, Elizabeth Czajka, Ross Goodwin, Kristina Pritchard, Michael Starkey, Ryan Sawyer, Christine Ray, and Jacob Nickell. The data presented here reside at NASA's Planetary Data System (<https://pds.nasa.gov/>). The data from the figures are publicly available on a permanent repository at the following address (<https://pubdata.space.swri.edu/look/0/51aacdee-b785-49f0-a60a--a4fc5cf0918e>). This work was funded by the NASA New Frontiers Program for Juno. The research at the University of Iowa is supported by NASA through Contract 699041X with the Southwest Research Institute.

- Bagenal, F., Wilson, R. J., Siler, S., Paterson, W. R., & Kurth, W. S. (2016). Survey of Galileo plasma observations in Jupiter's plasma sheet. *Journal of Geophysical Research: Planets*, *121*, 871–894. <https://doi.org/10.1002/2016JE005009>
- Barnhart, B. L., Kurth, W. S., Groene, J. B., Faden, J. B., Santolik, O., & Gurnett, D. A. (2009). Electron densities in Jupiter's outer magnetosphere determined from Voyager 1 and 2 plasma wave spectra. *Journal of Geophysical Research*, *114*, A05218. <https://doi.org/10.1029/2009JA014069>
- Bevington, P. R., & Robinson, D. K. (2003). *Data reduction and error analysis for the physical sciences*, (3rd ed.). McGraw-Hill, ISBN 0–07–247227-8: Boston, MA.
- Bolton, S. J., Lunine, J., Stevenson, D., Connerney, J. E. P., Levin, S., Owen, T. C., et al. (2017). *Space Science Reviews*, *213*(1–4), 5–37. <https://doi.org/10.1007/s11214-017-0429-6>
- Bonfond, B., Grodent, D., Gérard, J.-C., Stallard, T., Clarke, J. T., Yoneda, M., et al. (2012). Auroral evidence of Io's control over the magnetosphere of Jupiter. *Geophysical Research Letters*, *39*, L01105. <https://doi.org/10.1029/2011GL050253>
- Bonfond, B., Gustin, J., Gérard, J.-C., Grodent, D., Radioti, A., Palmaerts, B., et al. (2015). The far-ultraviolet main auroral emission at Jupiter—Part 1: Dawn-dusk brightness asymmetries. *Annales Geophysicae*, *33*, 1203. <https://doi.org/10.5194/angeo-33-1203-2015>
- Bordoni, F. (1971). Channel electron multiplier efficiency for 10–1000 eV electrons. *Nuclear Instruments and Methods*, *97*(2), 405–408. [https://doi.org/10.1016/0029-554X\(71\)90300-4](https://doi.org/10.1016/0029-554X(71)90300-4)
- Carlson, C. W., Pfaff, R. F., & Watzin, J. G. (1998). The Fast Auroral SnapshoT (FAST) mission. *Geophysical Research Letters*, *25*, 2013–2016. <https://doi.org/10.1029/98GL01592>
- Clark, G., Mauk, B. H., Haggerty, D., Paranicas, C., Kollmann, P., Rymer, A., et al. (2017). Energetic particle signatures of magnetic field-aligned potentials over Jupiter's polar regions. *Geophysical Research Letters*, *44*, 8703–8711. <https://doi.org/10.1002/2017GL074366>
- Clark, G., Tao, C., Mauk, B. H., Nichols, J., Saur, J., Bunce, E. J., et al. (2018). Precipitating electron energy flux and characteristic energies in Jupiter's main auroral region as measured by Juno/JEDI. *Journal of Geophysical Research: Space Physics*, *123*, 7554–7567. <https://doi.org/10.1029/2018JA025639>
- Clarke, J., Grodent, D., Cowley, S., Bunce, E., Zarka, P., Connerney, J., & Satoh, T. (2004). In F. Bagenal, T. E. Dowling, & W. B. McKinnon (Eds.), *Jupiter's aurora, in Jupiter: Planet, satellites, magnetosphere*. Cambridge: Cambridge University Press.
- Clarke, J. T., Ballester, G., Trauger, J., Ajello, J., Pryor, W., Tobiska, K., et al. (1998). Hubble Space Telescope imaging of Jupiter's UV aurora during the Galileo orbiter mission. *Journal of Geophysical Research*, *103*(E9), 20217–20236. <https://doi.org/10.1029/98JE01130>
- Connerney, J. E. P., Acuña, M. H., & Ness, N. F. (1981). Jovian current sheet and inner magnetosphere. *Journal of Geophysical Research*, *86*(A10), 8370–8384. <https://doi.org/10.1029/JA086iA10p08370>
- Connerney, J. E. P., Acuna, M. H., Ness, N. F., & Satoh, T. (1998). New models of Jupiter's magnetic field constrained by the Io flux tube footprint. *Journal of Geophysical Research*, *103*, 11,929–11,939. <https://doi.org/10.1029/97JA03726>
- Connerney, J. E. P., Adriani, A., Allegrini, F., Bagenal, F., Bolton, S. J., Bonfond, B., et al. (2017). Jupiter's magnetosphere and aurorae observed by the Juno spacecraft during its first polar orbits. *Science*, *356*(6340), 826–832. <https://doi.org/10.1126/science.aam5928>
- Connerney, J. E. P., Benn, M., Bjarno, J. B., Denver, T., Espley, J., Jorgensen, J. L., et al. (2017). The Juno magnetic field investigation. *Space Science Reviews*, *213*(1–4), 39–138. <https://doi.org/10.1007/s11214-017-0334-z>
- Connerney, J. E. P., Kotsiaros, S., Oliverson, R. J., Espley, J. R., Joergensen, J. L., Joergensen, P. S., et al. (2018). A new model of Jupiter's magnetic field from Juno's first nine orbits. *Geophysical Research Letters*, *45*, 2590–2596. <https://doi.org/10.1002/2018GL077312>
- Cowley, S. W. H., & Bunce, E. J. (2001). Origin of the main auroral oval in Jupiter's coupled magnetosphere-ionosphere system. *Planetary and Space Science*, *49*(10–11), 1067–1088. [https://doi.org/10.1016/S0032-0633\(00\)00167-7](https://doi.org/10.1016/S0032-0633(00)00167-7)
- Dahl, D. A. (2000). SIMION for the personal computer in reflection. *International Journal of Mass Spectrometry*, *200*, p3.
- Deconihout, B., Vurpillot, F., Bouet, M., & Renaud, L. (2002). Improved ion detection efficiency of microchannel plate detectors. *Review of Scientific Instruments*, *73*(4), 1734–1740. <https://doi.org/10.1063/1.1461882>
- Dumont, M., Grodent, D., Radioti, A., Bonfond, B., & Gérard, J.-C. (2014). Jupiter's equatorward auroral features: Possible signatures of magnetospheric injections. *Journal of Geophysical Research: Space Physics*, *119*, 10,068–10,077. <https://doi.org/10.1002/2014JA020527>
- Dunn, W. R., Branduardi-Raymont, G., Ray, L. C., Jackman, C. M., Kraft, R. P., Elsner, R. F., et al. (2017). The independent pulsations of Jupiter's northern and southern X-ray auroras. *Nature Astronomy*, *1*(11), 758–764. <https://doi.org/10.1038/s41550-017-0262-6>
- Ebert, R. W., Allegrini, F., Bagenal, F., Bolton, S. J., Connerney, J. E. P., Clark, G., et al. (2017). Spatial distribution and properties of 0.1–100 keV electrons in Jupiter's polar auroral region. *Geophysical Research Letters*, *44*, 9199–9207. <https://doi.org/10.1002/2017GL075106>
- Ebert, R. W., Greathouse, T. K., Clark, G., Allegrini, F., Bagenal, F., Bolton, S. J., et al. (2019). Comparing electron energetics and UV brightness in Jupiter's northern polar region during Juno Perijove 5. *Geophysical Research Letters*, *46*, 19–27. <https://doi.org/10.1029/2018GL081129>
- Elliott, S. S., Gurnett, D. A., Kurth, W. S., Mauk, B. H., Ebert, R. W., Clark, G., et al. (2018). The acceleration of electrons to high energies over the Jovian polar cap via whistler mode wave-particle interactions. *Journal of Geophysical Research: Space Physics*, *123*, 7523–7533. <https://doi.org/10.1029/2018JA025797>
- Funsten, H. O., Harper, R. W., & McComas, D. J. (2005). Absolute detection efficiency of space-based ion mass spectrometers and neutral atom imagers. *The Review of Scientific Instruments*, *76*, 053301. <https://doi.org/10.1063/1.1889465>
- Gérard, J.-C., Bonfond, B., Grodent, D., & Radioti, A. (2016). The color ratio-intensity relation in the Jovian aurora: Hubble observations of auroral components. *Planetary and Space Science*, *131*, 14–23. <https://doi.org/10.1016/j.pss.2016.06.004>
- Gérard, J.-C., Bonfond, B., Grodent, D., Radioti, A., Clarke, J. T., Gladstone, G. R., et al. (2014). Mapping the electron energy in Jupiter's aurora: Hubble spectral observations. *Journal of Geophysical Research: Space Physics*, *119*, 9072–9088. <https://doi.org/10.1002/2014JA020514>
- Gérard, J.-C., Bonfond, B., Mauk, B. H., Gladstone, G. R., Yao, Z. H., Greathouse, T. K., et al. (2019). Contemporaneous observations of Jovian energetic auroral electrons and ultraviolet emissions by the Juno spacecraft. *Journal of Geophysical Research: Space Physics*, *124*, 8298–8317. <https://doi.org/10.1029/2019JA026862>
- Gladstone, G. R., Persyn, S. C., Eterno, J. S., Walther, B. C., Slater, D. C., Davis, M. W., et al. (2017). The ultraviolet spectrograph on NASA's Juno mission. *Space Science Reviews*, *213*(1–4), 447–473. <https://doi.org/10.1007/s11214-014-0040-z>
- Gladstone, G. R., Waite, J. H. Jr., Grodent, D., Lewis, W. S., Crary, F. J., Elsner, R. F., et al. (2002). A pulsating auroral X-ray hot spot on Jupiter. *Nature*, *415*(6875), 1000–1003. <https://doi.org/10.1038/4151000a>
- Goruganthu, R. R., & Wilson, W. G. (1984). Relative electron detection efficiency of microchannel plates from 0–3 keV. *Review of Scientific Instruments*, *55*(12), 2030–2033. <https://doi.org/10.1063/1.1137709>
- Gray, R. L., Badman, S. V., Woodfield, E. E., & Tao, C. (2017). Characterization of Jupiter's secondary auroral oval and its response to hot plasma injections. *Journal of Geophysical Research: Space Physics*, *122*, 6415–6429. <https://doi.org/10.1002/2017JA024214>

- Greathouse, T.K., G.R. Gladstone, M.W. Davis, D.C. Slater, M.H. Versteeg, K.B. Persson, et al. (2013). Performance results from in-flight commissioning of the Juno Ultraviolet Spectrograph (Juno-UVS). Southwest Research Institute. This document is available upon request.
- Grodent, D. (2015). A brief review of ultraviolet auroral emissions on giant planets. *Space Science Reviews*, *187*(1–4), 23–50. <https://doi.org/10.1007/s11214-014-0052-8>
- Grodent, D., Bonfond, B., Yao, Z., Gérard, J.-C., Radioti, A., Dumont, M., et al. (2018). Jupiter's aurora observed with HST during Juno orbits 3 to 7. *Journal of Geophysical Research: Space Physics*, *123*, 3299–3319. <https://doi.org/10.1002/2017JA025046>
- Grodent, D., Clarke, J. T., Kim, J., Waite, J. H. Jr., & Cowley, S. W. H. (2003). Jupiter's main auroral oval observed with HST-STIS. *Journal of Geophysical Research*, *108*(A11), 1389. <https://doi.org/10.1029/2003JA009921>
- Grodent, D., Clarke, J. T., Waite, J. H. Jr., Cowley, S. W. H., Gérard, J. C., & Kim, J. (2003). Jupiter's polar auroral emissions. *Journal of Geophysical Research*, *108*(A10), 1366. <https://doi.org/10.1029/2003JA010017>
- Grodent, D., Waite, J. H. Jr., & Gérard, J. C. (2001). A self-consistent model of the Jovian auroral thermal structure. *Journal of Geophysical Research*, *106*, 12,933–12,952. <https://doi.org/10.1029/2000JA900129>
- Gustin, J., Bonfond, B., Grodent, D., & Gérard, J. C. (2012). Conversion from HST ACS and STIS auroral counts into brightness, precipitated power, and radiated power for H₂ giant planets. *Journal of Geophysical Research*, *117*, A07316. <https://doi.org/10.1029/2012JA017607>
- Gustin, J., Cowley, S. W. H., Gérard, J. -C., Gladstone, G. R., Grodent, D., & Clarke, J. T. (2006). Characteristics of Jovian morning bright FUV aurora from Hubble Space Telescope/Space Telescope Imaging Spectrograph imaging and spectral observations. *Journal of Geophysical Research*, *111*, A09220. <https://doi.org/10.1029/2006JA011730>
- Gustin, J., Feldman, P. D., Gérard, J.-C., Grodent, D., Vidal-Madjar, A., Ben Jaffel, L., et al. (2004). Jovian auroral spectroscopy with FUSE: Analysis of self-absorption and implications for electron precipitation. *Icarus*, *171*(2), 336–355. <https://doi.org/10.1016/j.icarus.2004.06.005>
- Gustin, J., Grodent, D., Gérard, J. C., & Clarke, J. T. (2002). Spatially resolved far ultraviolet spectroscopy of the Jovian aurora. *Icarus*, *157*(1), 91–103. <https://doi.org/10.1006/icar.2001.6784>
- Gustin, J., Grodent, D., Ray, L. C., Bonfond, B., Bunce, E. J., Nichols, J. D., & Ozak, N. (2016). Characteristics of north Jovian aurora from STIS FUV spectral images. *Icarus*, *268*, 215–241. <https://doi.org/10.1016/j.icarus.2015.12.048>
- Hess, S. L. G., Bonfond, B., Zarka, P., & Grodent, D. (2011). Model of the Jovian magnetic field topology constrained by the Io auroral emissions. *Journal of Geophysical Research*, *116*, A05217. <https://doi.org/10.1029/2010JA016262>
- Hill, T. W. (1979). Inertial limit on corotation. *Journal of Geophysical Research*, *84*(A11), 6554–6558. <https://doi.org/10.1029/JA084iA11p06554>
- Hill, T. W. (2001). The Jovian auroral oval. *Journal of Geophysical Research*, *106*(A5), 8101–8108. <https://doi.org/10.1029/2000JA000302>
- Huang, T. W., & Hill, T. W. (1989). Corotation lag of the Jovian atmosphere, ionosphere, and magnetosphere. *Journal of Geophysical Research*, *94*(A4), 3761–3765. <https://doi.org/10.1029/JA094iA04p03761>
- Kimura, T., Badman, S. V., Tao, C., Yoshioka, K., Murakami, G., Yamazaki, A., et al. (2015). Transient internally driven aurora at Jupiter discovered by Hisaki and the Hubble Space Telescope. *Geophysical Research Letters*, *42*, 1662–1668. <https://doi.org/10.1002/2015GL063272>
- Kimura, T., Nichols, J. D., Gray, R. L., Tao, C., Murakami, G., Yamazaki, A., et al. (2017). Transient brightening of Jupiter's aurora observed by the Hisaki satellite and Hubble Space Telescope during approach phase of the Juno spacecraft. *Geophysical Research Letters*, *44*, 4523–4531. <https://doi.org/10.1002/2017GL072912>
- Kotsiaros, S., Connerney, J. E. P., Clark, G., Allegrini, F., Gladstone, G. R., Kurth, W. S., et al. (2019). Birkeland currents in Jupiter's magnetosphere observed by the polar-orbiting Juno spacecraft. *Nature Astronomy*, *3*(10), 904–909. <https://doi.org/10.1038/s41550-019-0819-7>
- Kurth, W. S., Hospodarsky, G. B., Kirchner, D. L., Mokrzycki, B. T., Averkamp, T. F., Robison, W. T., et al. (2017). The Juno waves investigation. *Space Science Reviews*, *213*(1–4), 347–392. <https://doi.org/10.1007/s11214-017-0396-y>
- Kurth, W. S., Mauk, B. H., Elliott, S. S., Gurnett, D. A., Hospodarsky, G. B., Santolik, O., et al. (2018). Whistler mode waves associated with broadband auroral electron precipitation at Jupiter. *Geophysical Research Letters*, *45*, 9372–9379. <https://doi.org/10.1029/2018GL078566>
- Lane, R. O., & Zaffarano, D. J. (1954). Transmission of 0–40 keV electrons by thin films with application to beta-ray spectroscopy. *Physical Review*, *94*(4), 960–964. <https://doi.org/10.1103/PhysRev.94.960>
- Li, W., Thorne, R. M., Ma, Q., Zhang, X.-J., Gladstone, G. R., Hue, V., et al. (2017). Understanding the origin of Jovian diffuse auroral precipitation using Juno's first Perijove observations. *Geophysical Research Letters*, *44*, 10,162–10,170. <https://doi.org/10.1002/2017GL075545>
- Lin, Y., & Joy, D. C. (2005). A new examination of secondary electron yield data. *Surface and Interface Analysis*, *37*, 895–900. <https://doi.org/10.1002/sia.2107>
- Louarn, P., Allegrini, F., McComas, D. J., Valek, P. W., Kurth, W. S., André, N., et al. (2018). Observation of electron conics by Juno: Implications for radio generation and acceleration processes. *Geophysical Research Letters*, *45*, 9408–9416. <https://doi.org/10.1029/2018GL078973>
- Macau, J. P., Jamar, J., & Gardier, S. (1976). Review of the influence of radiations on channeltrons and channel plates. *IEEE Transactions on Nuclear Science*, *23*(6), 2049–2055. <https://doi.org/10.1109/TNS.1976.4328623>
- Mauk, B. H., Haggerty, D. K., Jaskulek, S. E., Schlemm, C. E., Brown, L. E., Cooper, S. A., et al. (2017). The Jupiter Energetic Particle Detector Instrument (JEDI) investigation for the Juno mission. *Space Science Reviews*, *213*(1–4), 289–346. <https://doi.org/10.1007/s11214-013-0025-3>
- Mauk, B. H., Haggerty, D. K., Paranicas, C., Clark, G., Kollmann, P., Rymer, A. M., et al. (2017). Discrete and broadband electron acceleration in Jupiter's powerful aurora. *Nature*, *549*(7670), 66–69. <https://doi.org/10.1038/nature23648>
- Mauk, B. H., Haggerty, D. K., Paranicas, C., Clark, G., Kollmann, P., Rymer, A. M., et al. (2017). Juno observations of energetic charged particles over Jupiter's polar regions: Analysis of monodirectional and bidirectional electron beams. *Geophysical Research Letters*, *44*, 4410–4418. <https://doi.org/10.1002/2016GL072286>
- Mauk, B. H., Haggerty, D. K., Paranicas, C., Clark, G., Kollmann, P., Rymer, A. M., et al. (2018). Diverse electron and ion acceleration characteristics observed over Jupiter's main aurora. *Geophysical Research Letters*, *45*, 1277–1285. <https://doi.org/10.1002/2017GL076901>
- Mauk, B. H., & Saur, J. (2007). Equatorial electron beams and auroral structuring at Jupiter. *Journal of Geophysical Research*, *112*, A10221. <https://doi.org/10.1029/2007JA012370>
- McComas, D. J., Alexander, N., Allegrini, F., Bagenal, F., Beebe, C., Clark, G., et al. (2017). The Jovian Auroral Distributions Experiment (JADE) on the Juno mission to Jupiter. *Space Science Reviews*, *213*(1–4), 547–643. <https://doi.org/10.1007/s11214-013-9990-9>

- McNutt, R. L., Belcher, J. W., & Bridge, H. S. (1981). Positive ion observations in the middle magnetosphere of Jupiter. *Journal of Geophysical Research*, *86*, 8319–8342. <https://doi.org/10.1029/JA086iA10p08319>
- McNutt, R. L. Jr., Belcher, J. W., Sullivan, J. D., Bagenal, F., & Bridge, H. S. (1979). Departure from rigid co-rotation of plasma in Jupiter's dayside magnetosphere. *Nature*, *280*(5725), 803. <https://doi.org/10.1038/280803a0>
- Nichols, J., & Cowley, S. (2004). Magnetosphere-ionosphere coupling currents in Jupiter's middle magnetosphere: Effect of precipitation-induced enhancement of the ionospheric Pedersen conductivity. *Annales Geophysicae*, *22*(5), 1799–1827. <https://doi.org/10.5194/angeo-22-1799-2004>
- Nichols, J. D., Badman, S. V., Bagenal, F., Bolton, S. J., Bonfond, B., Bunce, E. J., et al. (2017). Response of Jupiter's auroras to conditions in the interplanetary medium as measured by the Hubble Space Telescope and Juno. *Geophysical Research Letters*, *44*, 7643–7652. <https://doi.org/10.1002/2017GL073029>
- Nichols, J. D., Bunce, E. J., Clarke, J. T., Cowley, S. W. H., Gérard, J. -C., Grodent, D., & Pryor, W. R. (2007). Response of Jupiter's UV auroras to interplanetary conditions as observed by the Hubble Space Telescope during the Cassini flyby campaign. *Journal of Geophysical Research*, *112*, A02203. <https://doi.org/10.1029/2006JA012005>
- Nichols, J. D., Clarke, J. T., Gérard, J. C., Grodent, D., & Hansen, K. C. (2009). Variation of different components of Jupiter's auroral emission. *Journal of Geophysical Research*, *114*, A06210. <https://doi.org/10.1029/2009JA014051>
- Parkinson, C. D., Stewart, A. I. F., Wong, A. S., Yung, Y. L., & Ajello, J. M. (2006). Enhanced transport in the polar mesosphere of Jupiter: Evidence from Cassini UVIS helium 584 Å airglow. *Journal of Geophysical Research*, *111*, E02002. <https://doi.org/10.1029/2005JE002539>
- Radioti, A., Gérard, J.-C., Grodent, D., Bonfond, B., Krupp, N., & Woch, J. (2008). Discontinuity in Jupiter's main auroral oval. *Journal of Geophysical Research*, *113*, A01215. <https://doi.org/10.1029/2007JA012610>
- Radioti, A., Tomás, A. T., Grodent, D., Gérard, J. C., Gustin, J., Bonfond, B., et al. (2009). Correction to "Equatorward diffuse auroral emissions at Jupiter: Simultaneous HST and Galileo observations". *Geophysical Research Letters*, *36*, L09103. <https://doi.org/10.1029/2009GL038676>
- Ray, L. C., Ergun, R. E., Delamere, P. A., & Bagenal, F. (2010). Magnetosphere-ionosphere coupling at Jupiter: Effect of field-aligned potentials on angular momentum transport. *Journal of Geophysical Research*, *115*, A09211. <https://doi.org/10.1029/2010JA015423>
- Saur, J., Janser, S., Schreiner, A., Clark, G., Mauk, B. H., Kollmann, P., et al. (2018). Wave-particle interaction of Alfvén waves in Jupiter's magnetosphere: Auroral and magnetospheric particle acceleration. *Journal of Geophysical Research: Space Physics*, *123*, 9560–9573. <https://doi.org/10.1029/2018JA025948>
- Saur, J., Mauk, B. H., Mitchell, D. G., Krupp, N., Khurana, K. K., Livi, S., et al. (2006). Anti-planetward auroral electron beams at Saturn. *Nature*, *439*(7077), 699–702. <https://doi.org/10.1038/nature04401>
- Saur, J., Pouquet, A., & Matthaeus, W. H. (2003). An acceleration mechanism for the generation of the main auroral oval on Jupiter. *Geophysical Research Letters*, *30*(5), 1260. <https://doi.org/10.1029/2002GL015761>
- Schippers, P., Blanc, M., André, N., Dandouras, I., Lewis, G. R., Gilbert, L. K., et al. (2008). Multi-instrument analysis of electron populations in Saturn's magnetosphere. *Journal of Geophysical Research*, *113*, A07208. <https://doi.org/10.1029/2008JA013098>
- Szalay, J. R., Allegrini, F., Bagenal, F., Bolton, S., Clark, G., Connerney, J. E. P., et al. (2017). Plasma measurements in the Jovian polar region with Juno/JADE. *Geophysical Research Letters*, *44*, 7122–7130. <https://doi.org/10.1002/2017GL072837>
- Szalay, J. R., Bonfond, B., Allegrini, F., Bagenal, F., Bolton, S., Clark, G., et al. (2018). In situ observations connected to the Io footprint tail aurora. *Journal of Geophysical Research: Planets*, *123*, 3061–3077. <https://doi.org/10.1029/2018JE005752>
- Valek, P. W., Allegrini, F., Bagenal, F., Bolton, S. J., Connerney, J. E. P., Ebert, R. W., et al. (2019). Jovian high-latitude ionospheric ions: Juno in situ observations. *Geophysical Research Letters*, *46*, 8663–8670. <https://doi.org/10.1029/2019GL084146>
- Waite, J. H. Jr., Gladstone, G. R., Lewis, W. S., Goldstein, R., McComas, D. J., Riley, P., et al. (2001). An auroral flare at Jupiter. *Nature*, *410*(6830), 787–789. <https://doi.org/10.1038/35071018>
- Waite, J. H. Jr., et al. (2000). Multispectral observations of Jupiter's aurora. *Advances in Space Research*, *26*(10), 1453–1475. [https://doi.org/10.1016/S0273-1177\(00\)00089-2](https://doi.org/10.1016/S0273-1177(00)00089-2)
- Wilson, R. J. (2017). JADE standard product data record and archive volume software interface specification. PDS archive volume JNO-J/SW-JAD-3-CALIBRATED-V1.0 at <https://pds.nasa.gov/>
- Yao, Z. H., Grodent, D., Kurth, W. S., Clark, G., Mauk, B. H., Kimura, T., et al. (2019). On the relation between Jovian aurorae and the loading/unloading of the magnetic flux: Simultaneous measurements from Juno, Hubble Space Telescope, and Hisaki. *Geophysical Research Letters*, *46*, 11,632–11,641. <https://doi.org/10.1029/2019GL084201>